# Proximity proteomics reveals UCH-L1 as an NLRP3 interactor that modulates IL-1β production in human macrophages and microglia

Zhu Liang[1,2,12*], Andreas Damianou[1,2,12], Iolanda Vendrell[1,2], Edward Jenkins[3], Frederik H. Lassen[4], Sam J Washer[5,6], Guihai Liu[1], Gangshun Yi[7], Hantao Lou[8], Fangyuan Cao[9], Xiaonan Zheng[1], Ricardo A. Fernandes[1], Tao Dong[1], Edward W. Tate[9], Elena Di Daniel[10,11], Benedikt M Kessler[1,2*]

[1]Chinese Academy for Medical Sciences Oxford Institute, Nuffield Department of Medicine, University of Oxford, Roosevelt Drive, Oxford OX3 7FZ, UK

[2]Target Discovery Institute, Centre for Medicines Discovery, Nuffield Department of Medicine, University of Oxford, Roosevelt Drive, Oxford OX3 7FZ, UK

[3]Kennedy Institute of Rheumatology, University of Oxford, OX3 7FY UK

[4]Big Data Institute, Li Ka Shing Centre for Health Information and Discovery, Nuffield Department of Medicine, University of Oxford, Old Road Campus OX3 7LF, UK

[5]James and Lillian Martin Centre for Stem Cell Research, Sir William Dunn School of Pathology, University of Oxford, South Parks Road, Oxford, OX1 3RE, UK

[6]Wellcome Centre for Human Genetics, Nuffield Department of Medicine, University of Oxford, Oxford, UK

[7]Division of Structural Biology, Wellcome Trust Centre for Human Genetics, University of Oxford, Oxford OX3 7BN, UK

[8]Ludwig Institute for Cancer Research, University of Oxford, Oxford, UK

[9]Department of Chemistry, Molecular Sciences Research Hub, Imperial College London, London, W12 0BZ, UK

[10]Alzheimer's Research UK Oxford Drug Discovery Institute, University of Oxford, Oxford OX3 7FZ, United Kingdom

[11]Present address: Astex Pharmaceuticals, 436 Cambridge Science Park, Milton Rd, Milton, Cambridge CB4 0QA, UK

[12]Equal contribution

**Running title:** UCH-L1 regulates NLRP3 inflammasome & IL-1β production

***Corresponding author(s):** Zhu Liang, email: zhu.liang@ndm.ox.ac.uk

Benedikt M Kessler, email: benedikt.kessler@ndm.ox.ac.uk

**Key words**: Deubiquitylase, DUB, IL-1β, inflammasome, NLRP3, protease inhibitor, ubiquitin, UCH-L1

## ABSTRACT (149 words)

Activation of the NACHT, LRR family pyrin domain containing 3 (NLRP3) inflammasome complex is an essential innate immune signalling mechanism. To reveal how human NLRP3 inflammasome assembly and activation are controlled, in particular by components of the ubiquitin system, proximity labelling, affinity purification and RNAi screening approaches were performed. Our study provides an intricate time-resolved molecular map of different phases of NLRP3 inflammasome activation. Also, we show that ubiquitin C-terminal hydrolase 1 (UCH-L1) interacts with the NACHT domain of NLRP3. Downregulation of UCH-L1 decreases pro-IL-1β levels. UCH-L1 chemical inhibition with small molecules interfered with NLRP3 puncta formation and ASC oligomerization, leading to altered IL-1β cleavage and secretion, particularly in microglia cells, which exhibited elevated UCH-L1 expression as compared to monocytes/macrophages. Altogether, we profiled NLRP3 inflammasome activation dynamics and highlight UCH-L1 as an important modulator of NLRP3-mediated IL-1β production, suggesting that a pharmacological inhibitor of UCH-L1 may decrease inflammation-associated pathologies.

## INTRODUCTION

Innate immunity reflects a cornerstone of defence systems in living organisms which integrates with adaptive immune responses in the case of higher eukaryotes (Paludan et al., 2021). A major hallmark is the activation of inflammasome complexes, composed of ASCs and NLRs, such as NACHT, LRR family pyrin domain containing 3 (NLRP3) (Martinon et al., 2002) involving cleavage of pro-IL1β by caspase-1 (Gross et al., 2012). External stimuli including lipopolysaccharide (LPS) as the first, and nigericin, monosodium urate (MSU) monohydrate, Alum, ATP or cholesterol crystals as the second signal lead to the assembly and activation of the NLRP3 inflammasome complex, resulting in inflammatory responses (Shao et al., 2015; Swanson et al., 2019). Assembly of this supramolecular structure, featuring NLRP3 and ASC, is further regulated by associated factors, such as NEK7 (He et al., 2016), as well as specific posttranslational modifications including phosphorylation and ubiquitylation (Akther et al., 2021; Liang et al., 2021; Zangiabadi and Abdul-Sater, 2022). In addition to the kinases RIPK3 (Lawlor et al., 2015), FYN (Panicker et al., 2019) and ubiquitin ligases TRIM31(Song et al., 2016), gp78/Insig-1 (Xu et al., 2022), MARCH7 (Yan et al., 2015), HUWE1 (Guo et al., 2020), RNF25 and Cbl (Tang et al., 2020), deubiquitylases (DUBs) have been shown to modulate ubiquitylation of components of the inflammasome often in the context of specific diseases (Lopez-Castejon and Edelmann, 2016; Lopez-Castejon et al., 2013). More specifically, ubiquitylation and deubiquitylation of NLRP3 and IL-1β (Vijayaraj et al., 2021) have been reported to reflect critical checkpoints of NLRP3 inflammasome complex assembly, activation and signalling (Lopez-Castejon, 2020). Ubiquitin protease 7 (USP7) and 47 (USP47) inhibition resulted in reduced inflammasome activation (Palazon-Riquelme et al., 2018). In addition, in mice, BRCC3, a DUB reflecting a component

69 of the BRISC complex, was shown to deubiquitylate NLRP3, thereby regulating inflammasome activity
70 (Py et al., 2013). Recently, increasing number of findings suggest a complex interplay between
71 ubiquitylation and deubiquitylation mechanisms that modify components of the inflammasome
72 complex. However, most studies of ubiquitin-mediated NLRP3 pathway were conducted in murine
73 models, such as NG5, mouse peritoneal macrophages, and mouse bone marrow-derived macrophages
74 (BMDMs) (Py et al., 2013; Ren et al., 2019; Song et al., 2020). Given the inter-species divergence
75 between human and mouse inflammasome complexes and regulatory pathways, the role of
76 ubiquitylation/deubiquitylation in human NLRP3 inflammasome activation remains largely unknown.

77 To gain a more comprehensive understanding of the ubiquitin-mediated regulation of the human
78 NLRP3 inflammasome, we have combined ascorbic acid peroxidase 2 (APEX2)-based proximity
79 labelling, affinity purification and RNAi screening to discover molecular factors involved in the primary
80 and secondary signals of NLRP3 inflammasome activation and assembly. In both, a reconstituted
81 system and macrophages, we demonstrate that UCH-L1 interacts with the NACHT domain of NLRP3
82 and thereby interferes with ASC and NLRP3 assembly. Furthermore, ubiquitin C-terminal hydrolase 1
83 (UCH-L1) knockdown or chemical inhibition interferes with IL-1β production, particularly in microglia
84 cells that exhibited elevated UCH-L1 expression as compared to peripheral monocytes or macrophages.

85 **RESULTS**

86 **NLRP3-APEX2 captures the NLRP3 molecular proximity network**

87 As the N-terminus NLRP3 PYD domain has been reported to be responsible for initiating NLRP3
88 oligomerization, we inserted APEX2 at the C-terminus (LRR domain) of NLRP3 including a flexible
89 linker between these domains and a flag epitope at the N-terminus (**Figure 1A**). To avoid unstable
90 expression and mis-localization during transient transfection, we generated a NLRP3-APEX2 HEK293
91 stable cell line using the Flp-In T-REx system, allowing dose-dependent control of expression with
92 tetracycline (**Figures S1A, B**). Fluorescence microscopy confirmed that both flag-NLRP3 and flag-
93 NLRP3-APEX2 can form puncta in the perinuclear areas in response to nigericin stimulation, while the
94 fusion proteins are diffused across the cytosol in the resting state (**Figures S1C, D**). ASC
95 oligomerization assays with co-expression of adaptor protein ASC in stable cell lines proved that both
96 flag-NLRP3 and flag-NLRP3-APEX2 are competent to recruit ASC and induce its polymerization upon
97 stimulation with nigericin (**Figures S2A, B**). Taken together, these results indicate that APEX2 tagging
98 fused to the C-terminus of NLRP3 does not impede its ability to sense stimuli, particularly nigericin
99 induced potassium efflux, and recruit ASC to form oligomers.

100 We next investigated whether biotin labelling profiles are spatially restricted to the fusion bait. Live
101 HEK293 cells expressing NLRP3-APEX2 were treated with or without nigericin. Subsequently, cells
102 were treated with $H_2O_2$ in the presence of biotin-phenol, followed by rapid quenching, methanol fixation

103 and staining (**Figure 1B**). In contrast to the native control without $H_2O_2$ treatment, we observed robust
104 biotinylation by streptavidin-Alexa Fluor 488 imaging. Under unstimulated conditions, NLRP3-APEX2
105 was diffused across the cytosol, with biotinylated proteins following similar distribution pattern. Upon
106 nigericin treatment, NLRP3-APEX2 oligomerized to form puncta close to the nucleus, and we also
107 observed specks formed by biotin labelled proteins (**Figure 1C**). This partially suggests the spatial
108 specificity of NLRP3-APEX2 induced biotinylation.

109 The ability of APEX2 to efficiently label and capture the NLPR3 "proximitome" was assessed using
110 streptavidin immunoblotting and Coomassie blue staining, confirming the robust biotin labelling
111 activity of APEX2 fused to NLRP3 (**Figure 1D, Figure S3B**). Initially, we investigated whether
112 APEX2 is competent to capture the known NLRP3-interacting protein-NIMA-related kinase 7 (NEK7).
113 In contrast to the unlabelled negative control, we found that NLRP3-APEX2 specifically biotinylated
114 NEK7. Additionally, a substantial increase in NEK7 protein sequestration was observed in association
115 with activated NLRP3 (**Figure 1D**).

116 Given the rapid kinetic properties of APEX2 proximity labelling, we next sought to map the
117 spatiotemporally resolved "proximitome" of NLRP3 upon stimulation by nigericin across various time
118 intervals. Following mass spectrometric analysis, 3,478 proteins in total were detected across the
119 DMSO control and nigericin treatment for 30 min, 60 min and 90 min. To maximize the signal-to-noise
120 ratio and discriminate the bona fide interacting partners from the background contaminants, Bayesian
121 model-based algorithm SAINTexpress (Teo et al., 2014) was applied, yielding 800-1,100 high
122 confidence NLRP3 proximal proteins (**Figures 2A-B, Figure S3A**). Unsupervised principal component
123 analysis (PCA) showed the clustering and patterns of different protein subgroups (**Figure 2C**). High
124 correlation was observed between the three biological repeats within each group confirming the low
125 technical variation in this experiment (**Figure S3C**).

126 To assess the specificity of the NLRP3 proximity proteome, we next sought to check if the known
127 NLRP3 interactors or regulators are biotinylated and captured by APEX2. SAINT probability scoring
128 and simpler fold-change (FC) were calculated by the comparison of prey protein abundance between
129 the bait and negative beads control. Previously reported 83 human NLRP3 interactors, retrieved from
130 public interaction repository BioGrid (https://thebiogrid.org/, version 4.4.209) and the literature (**Table**
131 **S1**) (Oughtred et al., 2021; Oughtred et al., 2019; Stark et al., 2006) were mapped and plotted with
132 stringent thresholds (SAINT probability > 0.8, FC-A ≥ 1). After filtering, 14 known NLRP3 interactors
133 (16%) were discerned as high-confidence hits within the proximal proteomic data (**Figures 2D-H,**
134 **Figure S4**) confirming the enrichment of NLRP3-associated proteins.

135 **Temporal tracking of the NLRP3 proximity proteome**

136 To gain mechanistic and functional insights into the NLRP3 proximity proteome following nigericin
137 stimulation at various intervals, we conducted a gene ontology-biological process (GO term-BP)

138 enrichment analysis (**Figure 2I**). 13 shared terms, including viral translation, apoptotic cell death
139 regulation, stress granule assembly and mitosis-associated processes, were significantly enriched across
140 all four groups. In contrast to the unstimulated control, pathways related to "protein kinase D signalling"
141 and "mRNA binding regulation" were uniquely present after nigericin-exposure, consistent with prior
142 observations (Zhang et al., 2017). Intriguingly, the enrichment of "cellular response to arsenite ion" and
143 "regulation of stress granule disassembly" terms suggest a potential functional association between
144 inflammasome and stress granule formation. This connection was substantiated by previous reports of
145 the stress granule protein DDX3X as a pivotal mediator, modulating between apoptotic ASC speck
146 formation and pro-survival stress signalling (Fox and Man, 2019; Samir et al., 2019). In terms of GO
147 term-molecular function (GO term-MF) enrichment analysis, "GTP-dependent protein binding" and "1-
148 phosphatidylinostitol binding" were significantly enriched solely in the nigericin-60 min and nigericin-
149 90 min groups, suggesting that nigericin treatment might induce the recruitment of proteins associated
150 with the above two biological functions (**Figures S5A-C**). GO term-cellular components (CC) analysis
151 identified 16 common subcellular compartments or complexes, including COPII vesicle coat, ESCRT-
152 0 complex, and chaperone complex. Notably, three endocytic recycling-associated complexes,
153 including the endosome-associated recycling protein (EARP) complex, endosome to plasma transport
154 vesicle and Golgi-associated retrograde protein (GARP) complex, were significantly enriched solely in
155 nigericin-60 min and nigericn-90 min groups, suggesting that the NLRP3 complex may translocate to
156 trans-Golgi network (TGN) or endosome upon stimulation (**Figure S5D**). Similarly, the compartments
157 enrichment analysis identified another four complexes, including Dcp1-Dcp2, signal recognition
158 receptor, MAD1 and the cohesin I complex, which were only captured and enriched in the last two
159 timepoints of nigericin treatment (**Figures S6A-E**). We also performed tissue enrichment analysis, and
160 not surprisingly, poor tissue specificity was observed in either unstimulated or stimulated groups
161 (**Figure S5E**). To further explore the physiological and pathological biological processes, a reactome
162 pathway analysis was performed on the proximity proteome. The top 20 significantly enriched pathways
163 are shown as in **Figure S6F**. Notably, several innate immunity and virus infection associated pathways,
164 such as interleukin-6 signalling, MHC class I complex, and PP2A-mediated dephosphorylation of key
165 metabolic factors, were identified and enriched. Selected gene sets involved in the above pathways are
166 plotted in **Figures S6G-H**.

167 **Localization analysis reveals translocation of NLRP3 upon stimulation**

168 As the subcellular relocalization of NLRP3 and its underlying mechanism remain controversial
169 (Hamilton and Anand, 2019), we performed the localization analysis to assess the spatial properties of
170 NLRP3 inflammasome during complex assembly. After the filtering, normalization, and imputation,
171 we compared the relative abundance of biotinylated proteins in the unstimulated (DMSO) and
172 stimulated states (nigericin-90 min). The resulting volcano plot (**Figure S3F**) shows 103 proteins
173 enriched in the right quadrant for the stimulated state, while 104 proteins enriched in the left quadrant

174 for the resting state, with relatively stringent cut-off for fold change and false discovery rate
175 (log2[FC]≥0.5 or ≤-0.5, FDR≤ 0.05). GO term-CC enrichment analysis was performed on the
176 differentially enriched proteins in either condition. The proximity proteome under stimulated condition
177 showed high spatial specificity for Golgi apparatus, with 24 proteins falling into the GO-CC term
178 category-Golgi membranes (**Figures S3D-F, Table S2**). This is consistent with the previous
179 observation that NLRP3 is activated and recruited to dispersed trans-Golgi networks (dTGN) in
180 response to diverse stimuli (Bordon, 2019; Chen and Chen, 2018).

181 **Mapping stimulation-dependent NLRP3 interaction alterations using APEX2-PL and AP-MS**

182 Modulation of the NLRP3 local milieu during the activation process was further examined using an
183 integrated approach that combined NLRP3 APEX2 proximity labelling (PL) and affinity purification
184 mass spectrometry (AP-MS) (**Figure 3A**). For APEX2 PL-MS, the SAINTexpress analysis identified
185 848 (DMSO) and 833 (Nig-90min) proximal proteins, while 484 (DMSO) and 366 potential interacting
186 proteins were captured using the AP-MS method (**Figures 3A, B, Figures S7A-H**). There was relatively
187 small number of overlapping proteins between APEX2 and AP-MS possibly as a result of the
188 complementary nature of these two techniques (**Figures 3C, D**) and consistent with previous studies
189 comparing BioID and AP-MS (Lambert et al., 2015). Additionally, we sought to compare the proximal
190 proteome of NLRP3 under both resting and activation states. Following a rigorous filtration, seven
191 known NLRP3-interacting proteins were differentially enriched. Of these, five proteins (NEK7, MAVS,
192 PRKD1, PRKD2, and PRKD3, highlighted in red) enriched in the right quadrant are established positive
193 regulators of NLRP3. In contrast, EIF2AK2 and LYN (highlighted in green) in the left quadrant are
194 previously characterized inhibitory mediators. Interestingly, we noticed an increased labelling and
195 capture of NLRP3 under stimulated conditions, likely due to oligomerization (**Figure 3E**).

196 To gain a visual understanding of the interaction networks within the NLRP3 proximity proteome and
197 infer related biological insights, we performed a PPI network analysis. As for the nigericin stimulated
198 condition (**Figure 3F)**, we identified protein complexes including the NLRP3 inflammasome, NEK7,
199 MAVS, the SNARE complex, COPII vesicle coat, the signal recognition particle receptor complex and
200 the protein kinase D signalling complex. **Figure 3G** highlights the interaction networks linked to the
201 unstimulated state, in which the centrosome, the catenin complex, translational initiation factor, calcium
202 dependent serine kinase and the N-end rule proteasomal pathway were significantly enriched.

203 **NLRP3-associated DUBs identified by proximity proteome-guided RNAi screening**

204 The proximity proteome enabled us to capture several ubiquitin system components including 18 DUBs
205 in total (USP9X, USP8, USP5, USP47, USP32, USP24, USP19, USP15, USP14, USP10, USP1, UCH-
206 L1, PAN2, OTULIN, OTUID4, OTUB1, EIF3H and CYLD), which passed the stringent filtering criteria
207 (SAINT probability > 0.8, FC-A ≥ 1). Among the 18 enriched DUBs, 9 were consistently present in all
208 the four groups, and no marked difference was noted between the stimulated and unstimulated states

209 (**Figures 4A-E**). To complement this, we carried out a DUB library RNAi screen in PMA-differentiated
210 THP-1 cells, aiming to assess their influences on NLRP3 inflammasome priming and activation,
211 reflected by IL-1β production. In total, knockdown of 25 DUBs (outliers that surpass mean ± 1 standard
212 deviation, z score ≥1 or ≤-1, **Table S3**) were found to alter IL-1β levels in THP-1 cells treated with LPS
213 or LPS /nigericin (**Figures 4F-G**). A combination of proximity proteomics and RNAi screening revealed
214 7 DUBs showing effects in both assays (USP9X, USP8, USP14, USP10, UCH-L1, OTUB1 and OTUD4)
215 (**Figure 4H**). USP9X, USP14, and OTUB1 have already been reported to modulate the NLRP3
216 inflammasome (Hai et al., 2022; Xiang et al., 2023), suggesting additional NLRP3-associated DUBs
217 (USP8, USP10, OTUD4 and UCH-L1).
218

219 **UCH-L1 interacts with the NACHT domain of NLRP3 and affects IL-1β production**

220 Amongst these DUBs, UCH-L1 consistently affected IL-1β levels and showed high NLRP3 proximity
221 scores. Notably, the knockdown of UCH-L1 did not alter pro-IL-1β mRNA expression, while it
222 decreased protein levels and production of the mature form in THP-1 monocytes (**Figures 4I, J**) and
223 human PBMCs (**Figures 4K, L**). Expression of IL-6 and TNFα were also slightly suppressed in the
224 absence of UCH-L1 (**Figure S8B, C**), indicating that UCH-L1 might also play a role in the NF-κB-
225 regulated priming stage. As UCH-L1 is highly abundant in cells associated with the central nervous
226 system, we sought to investigate its role in brain resident immune cells, such as microglia, which also
227 express NLRP3 inflammasome components (**Figure S9**). Similarly to THP-1 and PBMC cells, UCH-
228 L1 deficiency markedly suppressed IL-1β production in the human microglial cell line HMC3 (**Figures**
229 **4M, N**).
230

231 The NLRP3-UCH-L1 interaction was identified through NLRP3-APEX2 proximity labelling (**Figure**
232 **5A**) and confirmed by immunoprecipitation (**Figure 5B**) in HEK293 cells. Notably, the interaction
233 between NLRP3 and UCH-L1 decreases upon nigericin stimulation (**Figure 5B**). To further determine
234 which domain within NLRP3 interacts with UCH-L1, we overexpressed flag-tagged full-length and
235 truncated NLRP3 in HEK293T cells. UCH-L1 interacted with the full-length NLRP3 and NACHT
236 domain of NLRP3 (**Figure 5C**). These results imply that the NACHT domain of NLRP3 directly or
237 indirectly provides a binding site for UCH-L1. Additionally, immunofluorescence revealed the
238 colocalization of NLRP3 with UCH-L1 in hiPSC-derived microglial cells (**Figures 5D, E**).
239

240 **UCH-L1 catalytic inhibition abrogates ASC assembly, NLRP3 inflammasome activation and IL-**
241 **1β processing**

242 To investigate how UCH-L1 modulates IL-1β processing and release, we selected a potent inhibitor-
243 IMP-1711-S (small molecule 27 in patent (Mark Kemp, 2017), **Figure 6A**) (Panyain et al., 2020;

244 Panyain et al., 2021) and tested its effect on NLRP3 inflammasome activation in THP-1, mouse bone
245 marrow-derived macrophages (BMDMs), human PBMCs, and hiPSC-derived microglial cells. Cells
246 were primed with LPS, pre-treated with IMP-1711-S and stimulated with the NLRP3 activator nigericin.
247 We observed that the treatment with IMP-1711-S inhibited the production of IL-1β in a concentration-
248 dependent manner in PMA-differentiated THP-1 (**Figure 6B**) and hiPSC-derived microglia (**Figures**
249 **6K, L**). Both, caspase-1 p10 and cleaved IL-1β levels were reduced in supernatants from IMP-1711-S-
250 treated THP-1 cells (**Figures 6C-E**), suggesting that the inhibitor exerts its effect on the activation of
251 the caspase-1 and IL-1β processing stage. IMP-1711-S potently inhibited the release of lactate
252 dehydrogenase (LDH) and blocked pyroptotic cell death induced by nigericin (**Figures 6F, G**).
253 Additionally, IMP-1711-S treatment did not affect pro-caspase-1 or pro-IL-1β expression in lysates in
254 the priming stage with LPS stimulation (**Figure 6C**). Further investigation of ASC oligomerization in
255 THP-1 cells through crosslinking of the insoluble lysate fraction revealed that while IMP-1711-S had
256 no impact on ASC expression in cell lysates, it substantially reduced oligomerized ASC levels post LPS
257 and nigericin stimulation (**Figure 6H**). Additionally, in HEK293 cells, IMP-1711-S markedly
258 downregulated the formation of NLRP3 specks in a concentration-dependent manner (**Figures 6I, J**).
259 Our findings underscore that UCH-L1 inhibition impedes NLRP3 inflammasome activation by
260 disrupting NLRP3 assembly and the speck formation, ultimately leading to decreased IL-1β production
261 (**Figure 7**).
262

263 ## DISCUSSION

264 The NLRP3 inflammasome is central to innate immunity, and a detailed understanding of its molecular
265 dynamics and interactome is highly sought after. We found that NLRP3 tolerates C-terminally tagged
266 APEX2, retaining its competence to biotinylate and capture known interacting partners of endogenous
267 NLRP3. Using complementary techniques, such as APEX2 PL-MS, AP-MS, and siRNA screening, we
268 traced the time-resolved PPI networks local to the NLRP3 inflammasome upon stimulation. This
269 approach offers a resource-rich map for further investigations of the molecular intricacies of NLRP3
270 inflammasome activation and revealed that UCH-L1 is involved in regulating IL-1β production.

271 ### Deconvolution of the NLRP3-APEX2 proximity proteome

272 A critical issue related to proximity labelling experiments is discrimination between true interactors and
273 background noise. Proteins captured by NLRP3-APEX2 proximity labelling can be categorized into four
274 groups: Type I-True interacting proteins that physically interact with NLRP3 and or other components
275 of the complex; Type II-Compartmental or proximal proteins in the local milieu of NLRP3 reflecting
276 transient interactions; Type III-non-specific proteins that stick to streptavidin beads; Type IV-physically
277 non-existing proteins detected in error. Type I and type II provide insights into the PPI network and
278 local milieu of NLRP3, but type III and type IV are considered false positives. To establish a high
279 confidence proximity proteome resource for NLRP3, a variety of approaches were used to filter out type

280 III and type IV contaminant proteins. A Bayesian model-based algorithm (SAINTexpress) was applied
281 to analyze the proximity labelling data with a SAINT probability score threshold of 0.8 and fold change
282 ≥ 2, yielding 800-1100 proximal proteins per group (**Figures 2C, E-H**). Furthermore, the unstimulated
283 state was used as a control, which helped us distinguishing the differentially regulated interacting
284 partners upon stimulation with nigericin, still yielding more than 800 proteins per biological condition,
285 consistent with the APEX2 enzyme affording a biotin labelling radius of ~ 10 nm in live cells (Qin et
286 al., 2021). With a stringent cut-off, our data identified 103 high-confidence putative NLRP3-associated
287 proteins enriched under activated conditions and 104 proteins enriched under inactivated conditions.
288 These included known interactors, such as NEK7, MAVS, PRKD1/2/3, LYN and EIF2AK2 (**Figure**
289 **3E**). We note that spatial references have been shown to enhance the deconvolution of PL data. However,
290 in our study, this was not applied as NLRP3 resides in multiple compartments and translocates to distinct
291 organelles upon activation (Hamilton and Anand, 2019). By integrating PL data with AP-MS and siRNA
292 screening, we established an alternative method for validating NLRP3-associated proteins.
293

294 **UCH-L1 is an essential mediator of NLRP3/ASC assembly and IL-1β production**

295 Ubiquitin modification controls multiple elements of the NLPR3 activation process and IL-1β
296 production (Lopez-Castejon, 2020). Through a DUB siRNA screen, we pinpointed four deubiquitylating
297 enzymes, TNFAIP3, CYLD, USP7, and STAMBP, already been linked to IL-1β signalling pathways
298 (**Figure 4G)** (Bednash et al., 2021; Duong et al., 2015; Palazon-Riquelme et al., 2018; Vande Walle et
299 al., 2014; Yang et al., 2020). However, the intricate nature of IL-1β processing, spanning multiple
300 regulatory stages, poses a challenge to precisely attribute the functional impacts of each DUB. For
301 instance, UCH-L3 and L5 were suggested to affect inflammasome activation and IL-1β production,
302 although in the context of infection (Kummari et al., 2015; Qu et al., 2020; Ramachandran et al., 2021).
303 UCH-L3 may act in the priming stage, whereas UCH-L5's role maybe less clear outside the context of
304 pathogen-driven NLRP3 inflammasome activation, consistent with the former, but not the latter, being
305 detected in our screen (**Fig. 4G**).
306 Here, we identified UCH-L1 as an NLRP3 interacting modulator of the inflammasome. It is a member
307 of the ubiquitin C-terminal hydrolase (UCH) family involved in neurodegeneration and cancer
308 metastasis (Ham et al., 2021; Liu et al., 2002; Mondal et al., 2022b). UCH-L1 is highly expressed in the
309 central nervous system, with low expression levels in most other tissues under normal physiology.
310 Dysregulation of UCH-L1 expression and mutations have been implicated in multiple
311 neurodegenerative diseases, such as Parkinson's disease, Huntington's disease, and recessive hereditary
312 spastic paraplegia (SPG79) (Mondal et al., 2022a). Also, several studies linked UCH-L1 to inflammation
313 or innate immunity. For instance, UCH-L1 deficiency markedly reduces the secretion of pro-
314 inflammatory cytokines, notably IL-6 and TNFα (Zhang et al., 2021). LDN57444, an isatin O-acyl
315 oxime small molecule inhibitor, has demonstrated efficacy in ameliorating LPS-induced sepsis in *in vivo*

316 models (Zhang et al., 2021), although other studies have cast doubt on the specificity or efficacy of this
317 compound against UCH-L1 (Panyain et al., 2020). Another study reported that UCH-L1 promoted M1
318 macrophages polarization via the PI3K/Akt signalling pathway (Huang et al., 2022). Consistent with
319 previous findings, UCH-L1 knockdown or inhibition yielded a significant decrease in pro-inflammatory
320 cytokine expression and secretion including IL-1β, IL-6 and TNFα in both, THP-1 and human primary
321 monocytes, reflecting interference in upstream signalling affecting the priming stage (**Figures 4I-L,**
322 **Figures S8, S10**). Furthermore, mRNA levels of IL-1β remain unchanged in the absence of UCH-L1,
323 suggesting that UCH-L1 affects IL-1β at the post-transcriptional or protein level (**Figure 4J**). Notably,
324 pharmacological inhibition of UCH-L1 affected ASC/NLRP3 assembly and IL-1β production, which
325 are part of the second inflammasome induction signal (**Figure 6**). Although the small molecule inhibitor
326 IMP-1711-S altered secreted active caspase-1 levels (**Figure 6E**), it does not seem to cross-react or
327 inhibit caspases directly (Panyain et al., 2020). Caspase-1 inhibitors also show a different specificity
328 profile towards TNFα release (Cao et al., 2022). UCH-L1 inhibition interferes with upstream events,
329 such as NLRP3 puncta formation and ASC oligomerization (**Figure 6**), the latter of which is
330 phenocopied by UCH-L1 knockdown (**Figure S11**). UCH-L1, found to be bound to the NACHT domain
331 of NLRP3, may act as a gating/editing factor to control the ubiquitylation status of multiple components,
332 such as NLRP3, ASC, Caspase-1 and IL-1β, required for NLRP3-ASC inflammasome complex
333 assembly (**Figure 7**). Preliminary results indicate that NLRP3's half-live is dependent on the ubiquitin-
334 proteasome pathway (**Figure S12**). However, NLRP3 associated ubiquitylation appears to be minimally
335 altered by UCH-L1, and NLRP3 protein levels are unaffected (**Figures S12, 13**), suggesting a more
336 structural role for UCH-L1 and/or its modulation of NLRP3 ubiquitination during assembly rather than
337 controlling turnover. Though speculative at this stage, such a putative structural and ubiquitylation
338 editing "gate keeping" process maybe in analogy to the role of UCH-L5/UCH37 in the 26S proteasome
339 complex, required for substrate deubiquitylation and ubiquitin recycling prior to substrate unfolding by
340 the 19S and entry into the 20S for destruction (Song et al., 2021; Vander Linden et al., 2015).
341
342 In conclusion, in this study, we provide a detailed NLRP3 inflammasome interaction map at different
343 physiological stages. UCH-L1 was identified and validated as an essential regulator involved in NLRP3
344 inflammasome activation and IL-1β production, affected by UCH-L1 chemical inhibition and
345 phenocopied by UCH-L1 deletion. Our results may have translational implications in exploring
346 pharmacological inhibition of UCH-L1 in neuroinflammation-associated pathology, which could
347 include dementia.

348 **Figure 1**

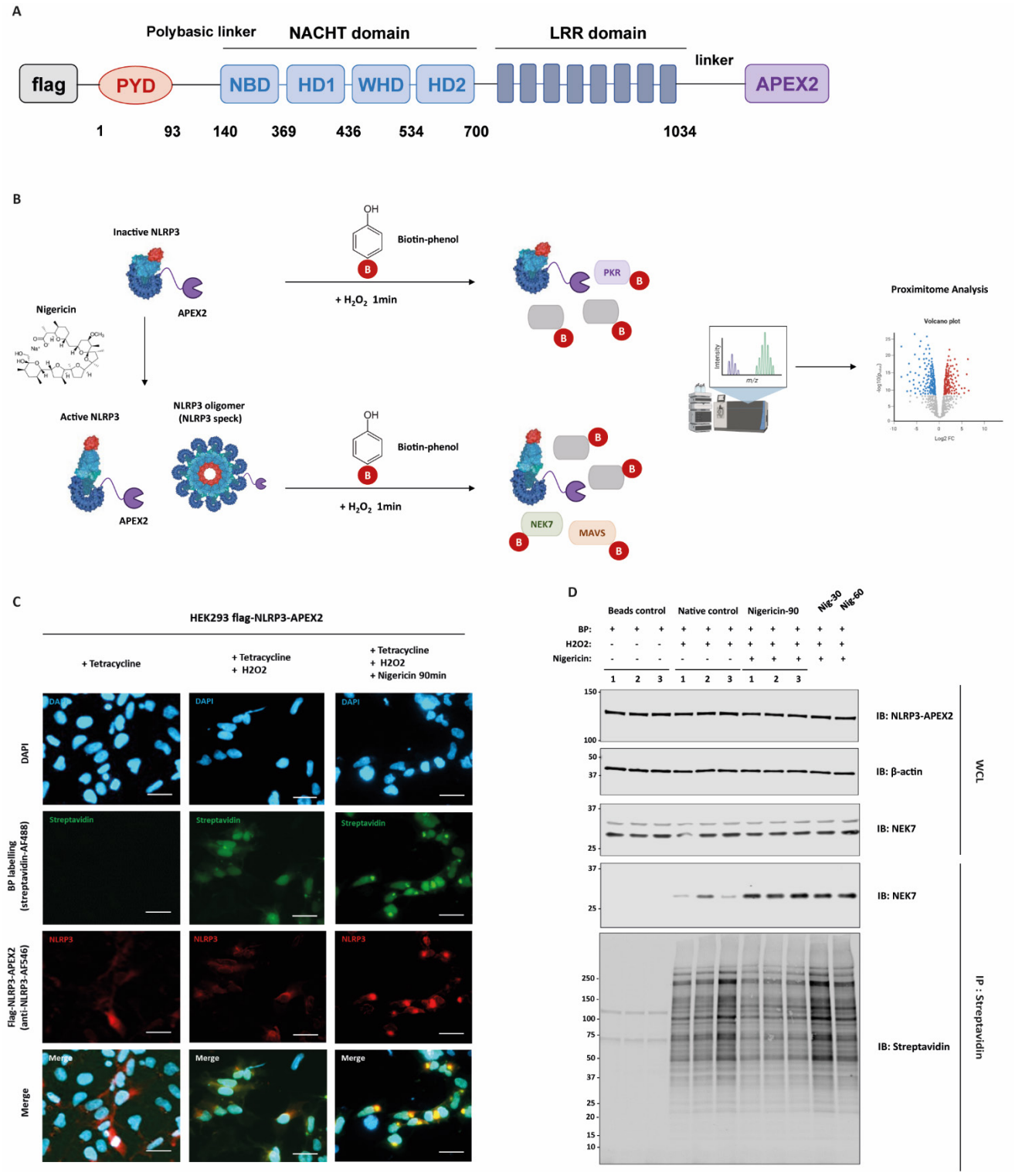


349

350 **Figure 1 | Proximity proteomic profiling of the NLRP3 inflammasome upon activation**

351 (A) Scheme of APEX2-tagging NLRP3. APEX2 was fused to the C terminus of full-length NLRP3 via
352 a glycine-serine linker. (B) Proximity labelling and mass spectrometric analysis workflow for NLRP3-
353 APEX2. (C) Confocal fluorescence imaging of NLRP3 APEX2 labelling in HEK293 cell lines. NLRP3-
354 APEX2 HEK293 stable cell lines were treated with tetracycline overnight, followed by the treatment

355 nigericin (10μM) or DMSO (control) for 90 min. Subsequently, cells were incubated with biotin phenol,
356 followed by $H_2O_2$ as indicated. Afterwards, cells were fixed and stained with streptavidin-Alexa Fluor
357 488 (AF488) conjugate to visualize biotinylated proteins and anti-NLRP3 antibody to visualize the
358 localization of NLRP3-APEX2. BP, biotinylated proteins. Scale bars, 50 μm. (D) Immunoblot showing
359 the biotinylated NEK7 captured by streptavidin beads in negative control, unstimulated and nigericin-
360 stimulated HEK293 Flp-In T-REx NLRP3-APEX2 cells. Cells were treated with tetracycline overnight,
361 and stimulated with nigericin for 30 min, 60 min, and 90 min before the APEX2 labelling. Whole cell
362 lysates and streptavidin pull-down were collected and blotted for NLRP3 and NEK7.

363

364

365

366

367

368

369

370

371

372

373

374

375

376

377

378

379

**Figure 2**

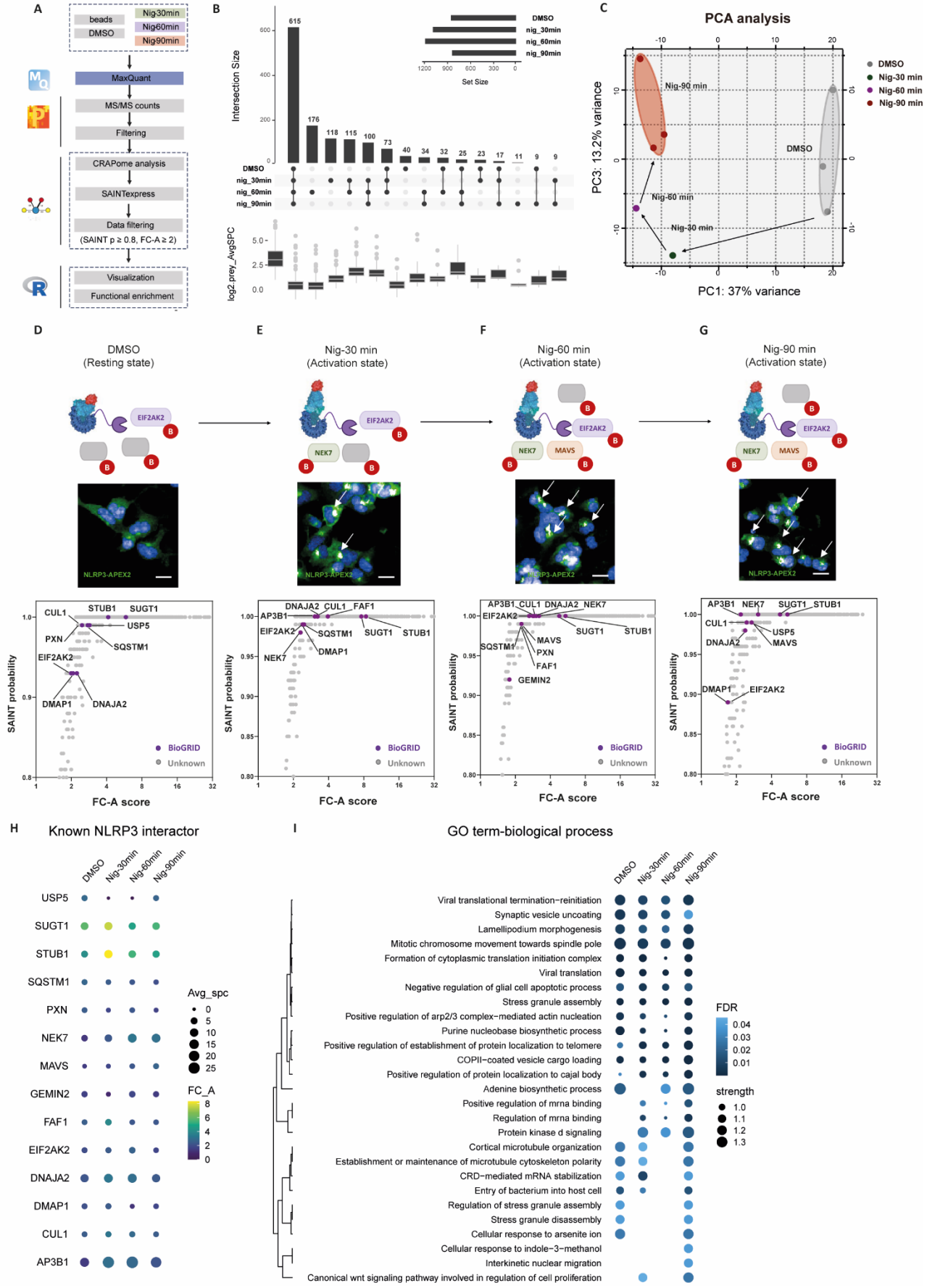
A
beads
DMSO
Nig30min
Nig60min
Nig90min
MaxQuant
MS/MS counts
Filtering
CRAPome analysis
SAINTexpress
Data filtering
(SAINT p ≥ 0.8, FC-A ≥ 2)
Visualization
Functional enrichment
B
Intersection Size
Set Size
log2.prey_AvgSPC
C
PCA analysis
PC3: 13.2% variance
PC1: 37% variance
Nig-90 min
Nig-60 min
Nig-30 min
DMSO
Nig-30 min
Nig-60 min
Nig-90 min
D
DMSO
(Resting state)
E
Nig-30 min
(Activation state)
F
Nig-60 min
(Activation state)
G
Nig-90 min
(Activation state)
EIF2AK2
NEK7
MAVS
NLRP3-APEX2
SAINT probability
FC-A score
BioGRID
Unknown
H
Known NLRP3 interactor
DMSO
Nig-30min
Nig-60min
Nig-90min
USP5
SUGT1
STUB1
SQSTM1
PXN
NEK7
MAVS
GEMIN2
FAF1
EIF2AK2
DNAJA2
DMAP1
CUL1
AP3B1
Avg_spc
FC_A
I
GO term-biological process
Viral translational termination−reinitiation
Synaptic vesicle uncoating
Lamellipodium morphogenesis
Mitotic chromosome movement towards spindle pole
Formation of cytoplasmic translation initiation complex
Viral translation
Negative regulation of glial cell apoptotic process
Stress granule assembly
Positive regulation of arp2/3 complex−mediated actin nucleation
Purine nucleobase biosynthetic process
Positive regulation of establishment of protein localization to telomere
COPII−coated vesicle cargo loading
Positive regulation of protein localization to cajal body
Adenine biosynthetic process
Positive regulation of mrna binding
Regulation of mrna binding
Protein kinase d signaling
Cortical microtubule organization
Establishment or maintenance of microtubule cytoskeleton polarity
CRD−mediated mRNA stabilization
Entry of bacterium into host cell
Regulation of stress granule assembly
Stress granule disassembly
Cellular response to arsenite ion
Cellular response to indole−3−methanol
Interkinetic nuclear migration
Canonical wnt signaling pathway involved in regulation of cell proliferation
FDR
strength

382 **Figure 2 | Temporal tracking of the NLRP3 proximity proteome**

383 (A) Schematic illustration of the data analysis for APEX2 PL-MS. (B) The upset plot depicting the
384 intersections of high confidence NLRP3 proximal proteins across samples. The bars in the y axis
385 represent the number of high confidence proximal proteins (SAINT probability score ≥ 0.8, fold change
386 ≥ 2) identified in each sample. The boxplot represents the log2 (average of spectral counts) of the
387 proximal proteins identified in each group. The median, first and third quartiles of the data were
388 displayed as the centre line, the lower and upper boundaries. (C) Principal component analysis of the 8
389 samples (3 unstimulated DMSO controls, 3 stimulated samples with 90 min treatment of nigericin,
390 30min nigericin-stimulated samples, and 60 min nigericin-stimulated samples). Each dot represents an
391 individual samples. (D-G) SAINT probability scoring of the proteomic data for NLRP3-APEX2
392 compared to the negative beads control. Proteins passing the cut off (SAINT probability score ≥ 0.8 and
393 FC-A score ≥ 1) are considered as high confidence proximal proteins for NLRP3. Previously reported
394 NLRP3-interacting proteins (BioGRID, v4.4.213) are coloured in purple. All other proteins are shown
395 in grey. (H) Dot plot of previously reported NLRP3-interacting proteins that are detected in the NLRP3-
396 APEX2 proximitome upon nigericin stimulation for different time points (unstimulated, 30 min, 60 min,
397 and 90 min). Sizes denote the average spectral counts and colours denote the FC-A score. (I) Dot plots
398 displaying the GOBP enrichment analysis of high confidence NLRP3 proximal proteins upon nigericin
399 stimulation for different timepoints as indicated.
400
401
402
403
404
405
406
407
408
409
410
411
412
413
414
415
416

417 **Figure 3**

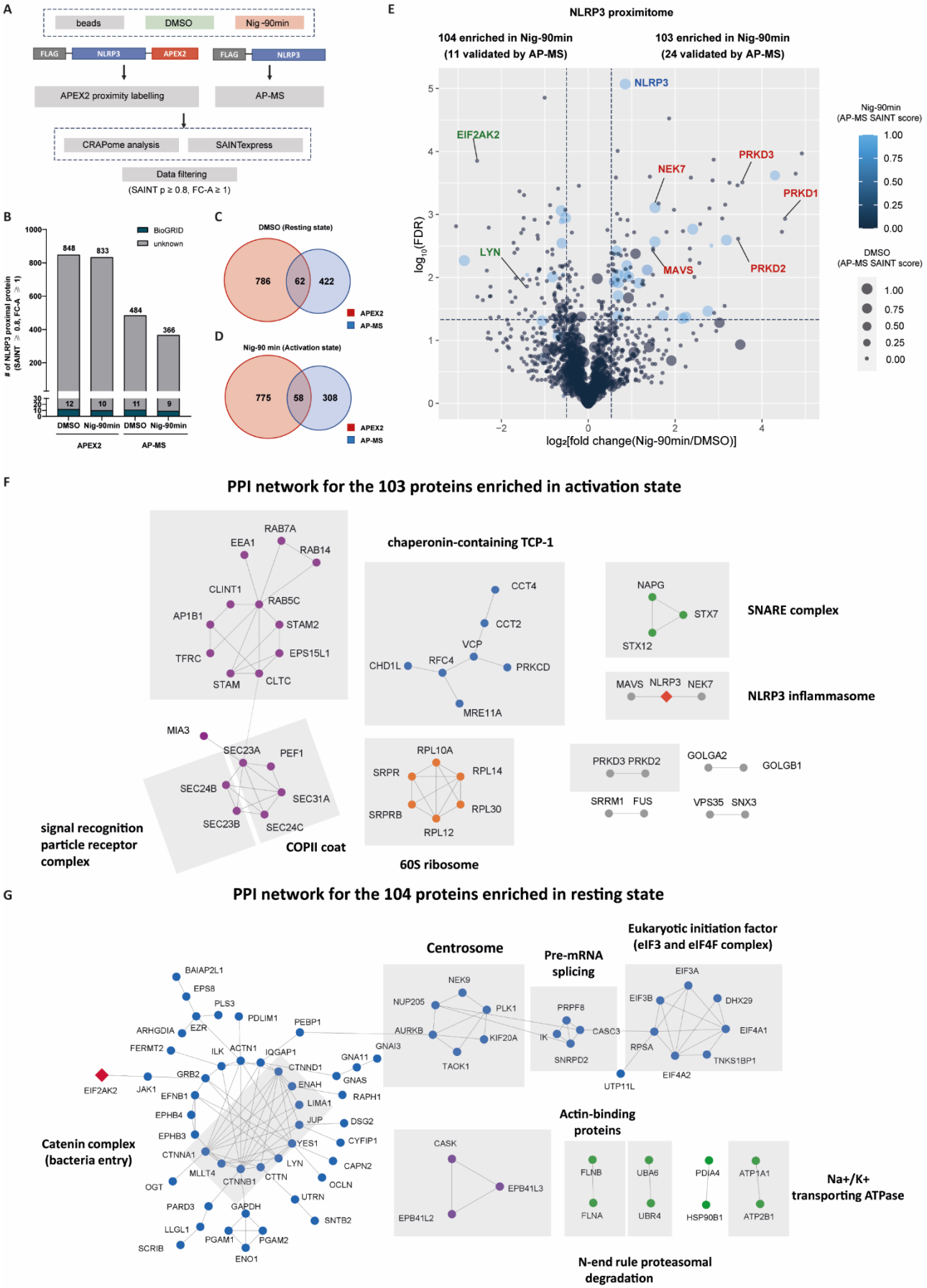


418

**Figure 3 | Mapping stimulation-dependent NLRP3 PPI alterations using APEX2-PL and AP-MS**

(A) Schematic of the integrated approach combining APEX2 proximity labelling and AP-MS. (B) The number of known (BioGRID, blue) and newly discovered NLRP3-interacting proteins (grey) from APEX2 proximity labelling or AP-MS. (C-D) Venn diagrams showing the number of NLRP3 proximal proteins identified in APEX2 proximity labelling or AP-MS. (E) Volcano plot depicting the fold change for relative protein quantification of NLRP3-APEX2 proximity labelling samples between unstimulated (DMSO) and stimulated conditions (nigericin-90min). Data are shown as means of three independent samples. Non-adjusted unpaired two-tailed t-test was applied to the statistical analysis. Sizes denote the SAINT probability score for AP-MS during stimulation (nigericin-90min), and colours reflect the score in its unstimulated condition. (F-G) Protein-protein interaction network for NLRP3-APEX2 proximity labelled proteins enriched after stimulation with nigericin (F) or unstimulated as control (G). MCL algorithm was performed with the PPI scores from STRING database (confidence score threshold = 0.7). Grey lines denote the high-confidence protein-protein interaction curated from Reactome, CORUM and IntAct database. Cluster labels were added manually. n = 3 biological replicates.

456 **Figure 4**

457

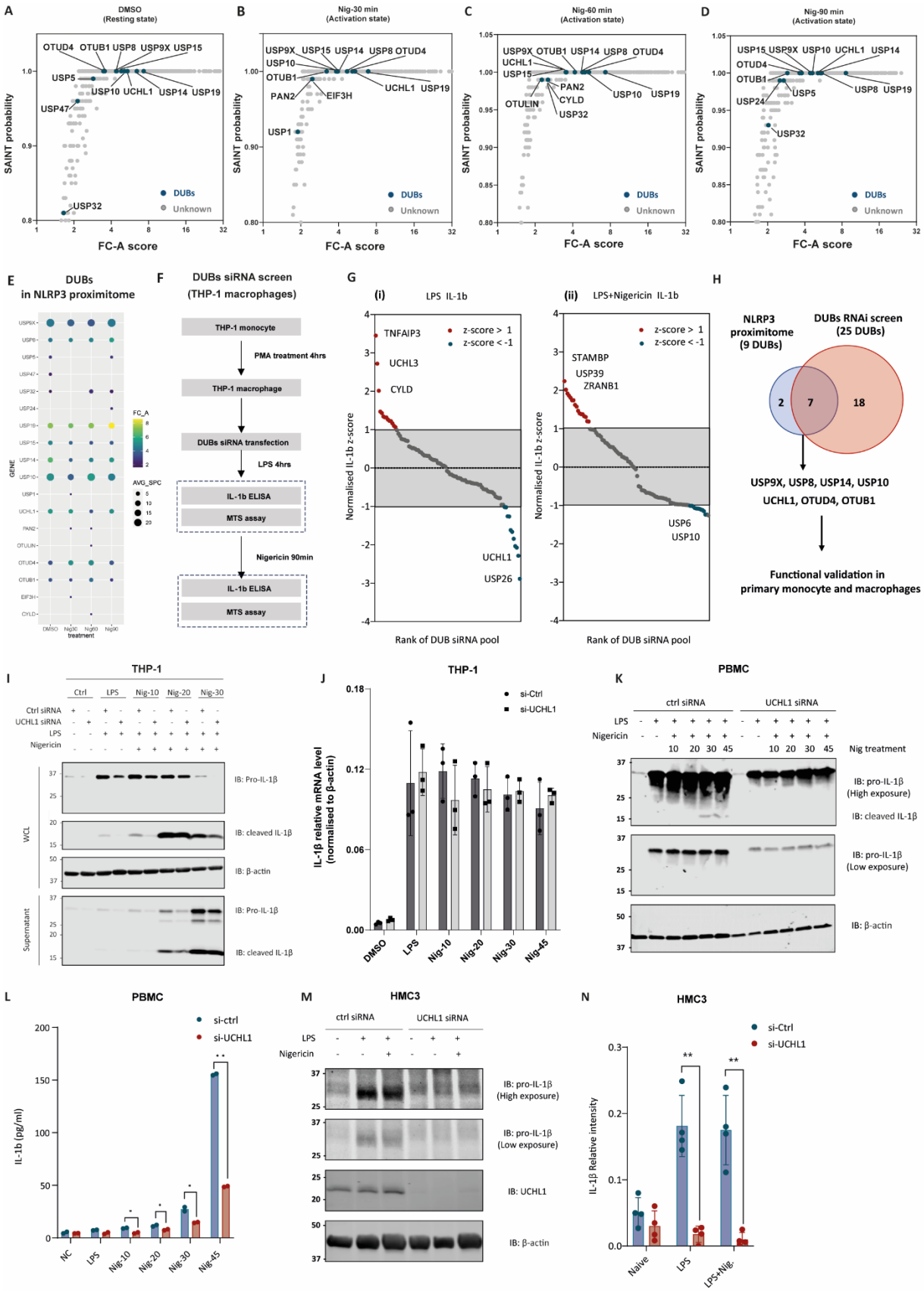


458

459 **Figure 4 | Proximity proteome-guided RNAi screen identifies deubiquitinases that are involved in**
460 **IL-1β production**

461 (A-D) APEX2 proximity labelling identifies DUBs in the local milieu of NLRP3 upon nigericin
462 stimulation. SAINT probability scoring of the proteomic data for NLRP3-APEX2 compared to the
463 negative beads control. Proteins passing the cut off (SAINT probability score ≥ 0.8 and FC-A score ≥
464 1) are considered as high confidence proximal proteins for NLRP3. Deubiquitinases are coloured in
465 blue and all other proteins are shown in grey. (E) Dot plots showing the DUBs in the NLRP3 proximity
466 proteome upon nigericin stimulation for different time points as indicated. Sizes denote the average
467 spectral counts and colours denote the FC-A score. (F) Schematic of experimental design for the DUB
468 siRNA library screen. (G) z-scores distribution of the IL-1β in the supernatant for individual siRNAs.
469 The RNAi screen is carried out in PMA-differentiated THP-1 cells upon LPS (i) or LPS+NIG treatment
470 (ii), using ELISA for the measurement of IL-1β in the supernatant. Hits with a z-score of ≤ -1 or ≥1 are
471 chosen as candidates for further validation. (H) Venn diagrams showing the intersection between the
472 hits identified through APEX2-PL and siRNA screen. (I-J) Immunoblot and RT-qPCR analysis of
473 whole cell lysates and supernatants from THP-1 cells transfected with non-targeting control siRNA, or
474 UCH-L1-specific siRNA. Cells were differentiated with PMA and primed with LPS (1 μg/mL) for 4
475 hours, followed by the treatment of nigericin (10 μM) for different timepoints as indicated. (K-L)
476 PBMCs were transfected with non-targeting control, or UCH-L1-specific siRNA, stimulated with LPS
477 for 4 hours and nigericin for different timepoints as indicated. (K) Immunoblot of cell lysates from
478 PBMCs. (L) Production of IL-1β in the supernatants from PBMCs as measured by ELISA. *$p < 0.05$,
479 **$p < 0.01$ (unpaired two-sided t-test). The results are representative of 3 independent experiments. (M-
480 N) Immunoblot of cell lysates from HMC3 cells transfected with non-targeting control siRNA or UCH-
481 L1-specific siRNA. Cells were primed with LPS (1 μg/mL) for 4 hours, followed by the treatment of
482 nigericin (10 μM) for 45 minutes. (N) IL-1β bands were quantified using GelAnalyzer and normalised
483 using β -actin bands. Error bars show the standard deviation of the mean. **$p < 0.01$ (unpaired two-
484 sided t-test).

485

486

487

488

489

490

491

492 **Figure 5**

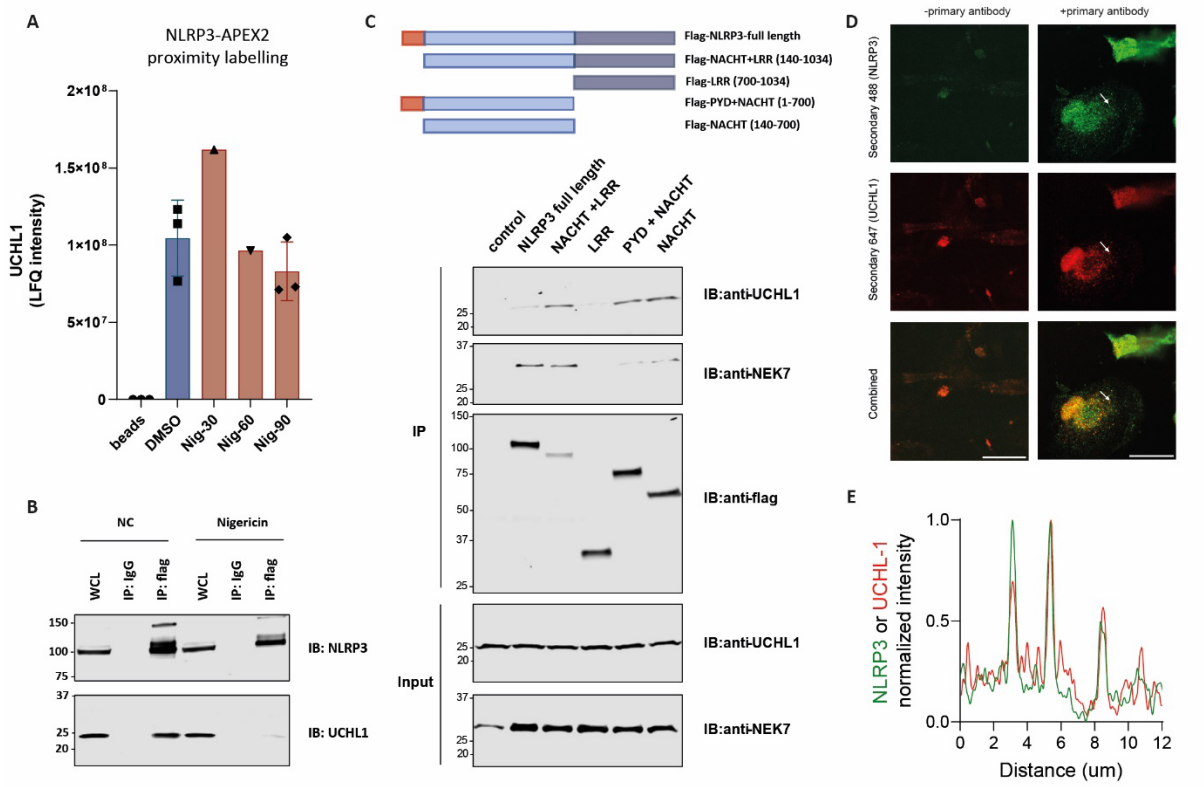


493

494 **Figure 5 | UCH-L1 interacts with the NACHT domain of NLRP3**

495 (A) The raw LFQ Intensity of UCH-L1 protein identified in the APEX2 proximity labelling performed
496 in this study across all the samples including beads Control, DMSO Control and Nigericin treatment at
497 different time points. Experiment was performed in triplicate except of Nig-30 and Nig-60 where only
498 1 replicant was performed. (B) Flp-In T-Rex 293 NLRP3-flag stable cells were induced with
499 tetracycline overnight. Afterwards, cells were treated with DMSO or Nigericin for 90 minutes. NLRP3-
500 flag was pulled down using anti-flag antibody or IgG and immunoblotted with indicated antibodies. (C)
501 Schematic representation of the N-terminal Flag-tagged NLRP3 domain constructs: full length NLRP3,
502 NACHT and LRR domain NLRP3 (Flag-NACHT+LRR, amino acids 140-1034), LRR domain of
503 NLRP3 (Flag-LRR, amino acids 700-1034), pyrin and NACHT domain of NLRP3 (Flag-
504 PYD+NACHT, amino acids 1-700), NACHT domain of NLRP3 (Flag-NACHT, amino acids 140-700).
505 HEK293T cells were transfected with the appropriate NLRP3 plasmid using Lipofectamine 3000. Cells
506 were cultured for 24 hours before they were lysed. NLRP3 domain-flag was pulled down using anti-
507 flag antibody and immunoblotted with indicated antibodies. (D) Fluorescence confocal images of
508 hiPSC-derived microglial cells stained for UCHL-1 and NLPR3. UCHL-1 and NLRP3 show
509 colocalization, but only when cells were stained with primary antibodies for UCHL-1 and NLRP3 (right
510 column). No colocalization is shown when cells are not stained with primary antibodies against UCHL-
511 1 and NLRP3 (left column). (E) Line profile showing the min-max normalized intensity of UCHL-1

512 (red) and NRLP3 (green) along and in the direction of the white arrow indicated in (D). The peaks in
513 normalized intensity indicate colocalization of NLRP3 and UCHL-1 in enriched areas (or 'specks') of
514 NLRP3.
515
516
517
518
519
520
521
522
523
524
525
526
527
528
529
530
531
532
533
534
535
536
537
538

539 **Figure 6**

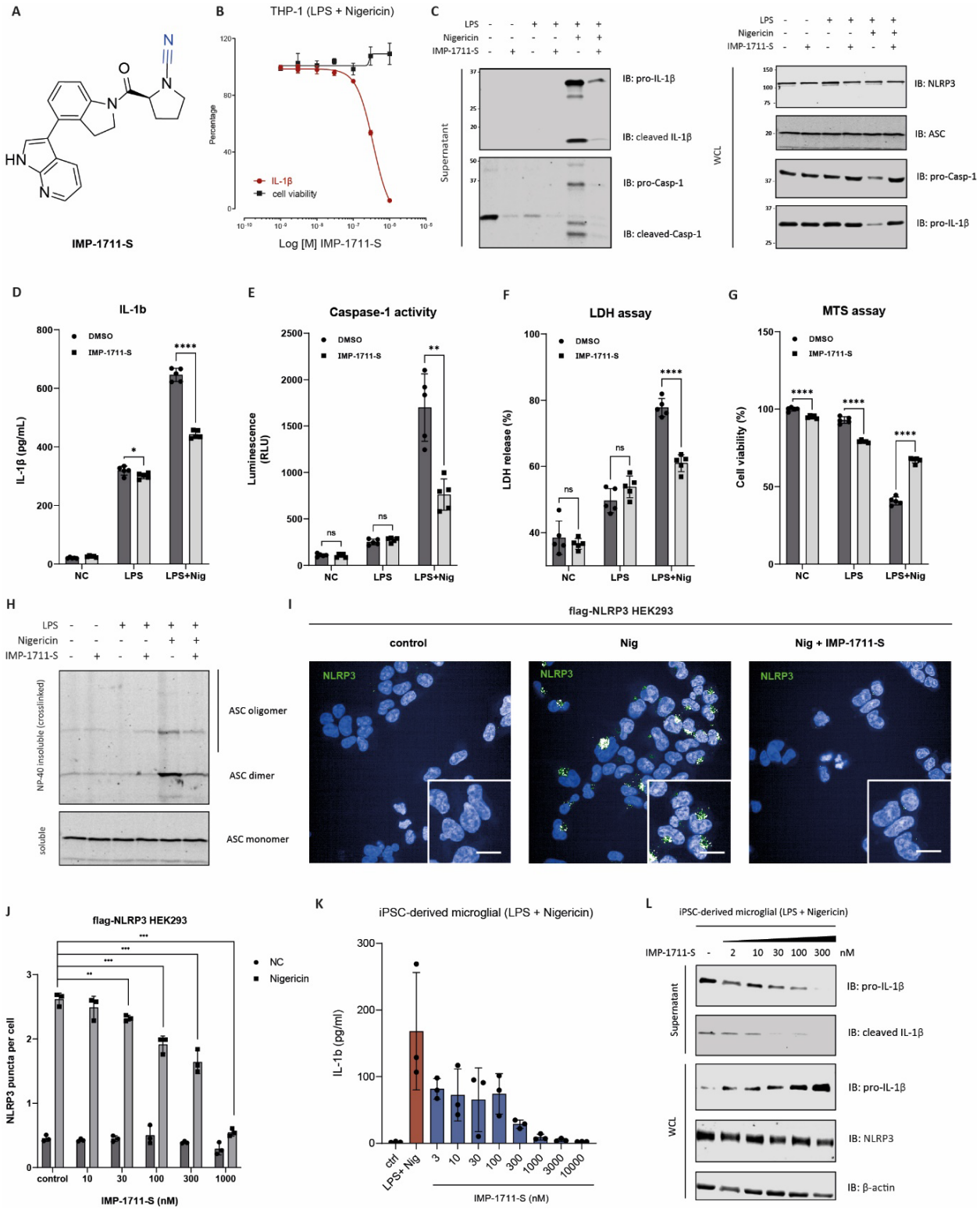


540

541

542

543

544 **Figure 6 | UCH-L1 inhibitor blocks ASC/NLRP3 assembly and IL-1β production**
545 (A) UCH-L1 inhibitor IMP-1711-S structure. (B) Red, production of IL-1β from PMA-differentiated
546 THP-1 cells stimulated with LPS and nigericin and treated with IMP-1711-S (3-10,000 nM) as measure
547 by ELISA (red). Black, cell viability measured by MTS assay. Data are expressed as mean ± s.d., n = 3
548 biologically independent samples. (C-G) THP-1 cells were differentiated with PMA and primed with
549 LPS (1 μg/mL) for 4 hours, followed by the treatment of nigericin (10 μM) for 45 minutes. DMSO or
550 IMP-1711-S (0.3 μM) was added at the same time with LPS. (C) Immunoblot analysis of whole cell
551 lysates and supernatants from THP-1 cells treated with DMSO or IMP-1711-S. (D-E) Supernatants
552 were collected for the measurement of IL-1β (D), Caspase-1 activity (E) from 3 independent
553 experiments. *$p < 0.05$, **$p < 0.01$, ***$p < 0.001$, ****$p < 0.0001$ (unpaired two-sided t-test).
554 Additionally, the cell viability was measured using LDH assay (F) and MTS assay (G). (H) Immunoblot
555 analysis of ASC polymerization upon treatment of DMSO or IMP-1711-S. (I-J) Immunofluorescence
556 imaging of flag-NLRP3 HEK293 stable cells treated with DMSO or IMP-1711-S (300nM), followed
557 by the stimulation with nigericin. Scale bars, 10 μm. (J) Quantitative analysis of the NLRP3 puncta
558 formation upon nigericin treatment in the presence of DMSO or different doses of IMP-1711-S (0.001-
559 1μM) as indicated. **$p < 0.01$, ***$p < 0.001$. (K) IL-1β levels were determined using ELISA from the
560 supernatant of fully differentiated hiPSC-derived microglia. Cells were primed with LPS (1 μg/mL) for
561 4 hours, followed by the treatment of nigericin (10 μM) for 45 minutes. IMP-1711-S inhibitor was
562 added simultaneously with LPS at different concentrations. (L) Immunoblot analysis of whole cell
563 lysates and supernatants from hiPSC-derived microglia treated with DMSO or different concentrations
564 of IMP-1711-S as indicated.

565

566

567

568

569

570

571

572

573

574

575

576 **Figure 7**

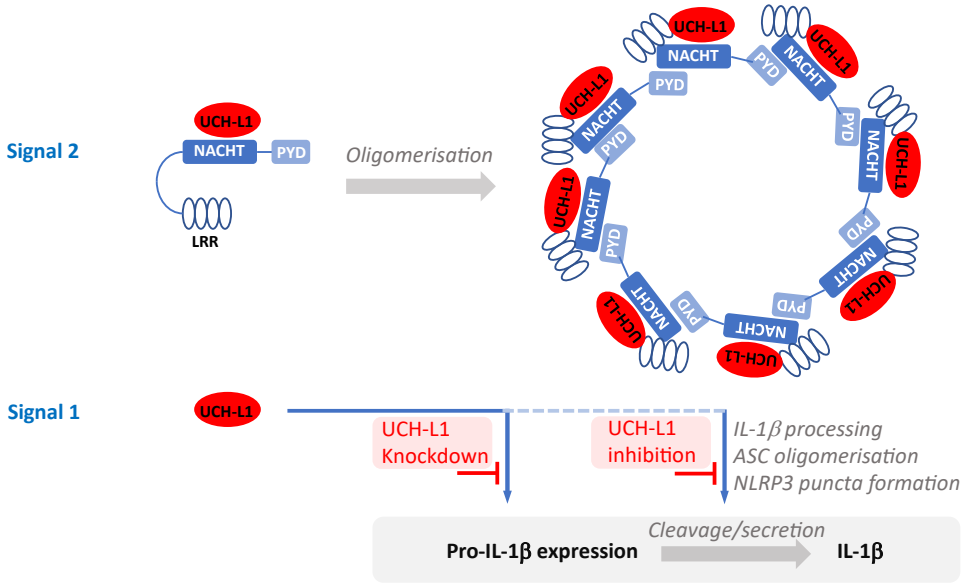


577

578 **Figure 7 | Model illustrating multi-functional roles of UCH-L1 in the NLRP3-mediated IL-1β**
579 **expression, processing and production.** UCH-L1 was shown previously to play a role in NF-κB
580 signalling, affecting pro-IL-1β expression (Zhang et al., 2021) in the context of signal 1. UCH-L1
581 deletion or pharmacological inhibition interferes with IL-1β production through processes of signal 2
582 (nigericin) involving ASC oligomerisation, thereby blocking IL-1β processing and secretion.

583

584

585 **STAR★Methods**

586 **Key resources table**

| REAGENTS or RESOURCE | SOURCE | IDENTIFIER |
|---|---|---|
| **Antibodies** | | |
| Cleaved IL-1 β (Asp116) | Cell Signalling Technology | CAT# 83186 |
| IL-1β | Cell Signalling Technology | CAT# 12703 |
| Caspase-1 | Cell Signalling Technology | CAT# 2225 |
| NLRP3 | Cell Signalling Technology | CAT# 15101 |
| ASC(B-3) | Santa Cruz | CAT# sc-514414 |
| β-Actin | Sigma-Aldrich | CAT# A5441 |
| NEK7 | Abcam | CAT# ab133514 |
| UCHL1 | Santa Cruz | CAT# sc-271639 |
| IRDye® 800CW Goat anti-Rabbit IgG Secondary Antibody | LI-COR | CAT# 926-32211 |
| IRDye® 800CW Goat anti-Mouse IgG Secondary Antibody | LI-COR | CAT# 926-32210 |
| IRDye® 680RD Goat anti-Mouse IgG Secondary Antibody | LI-COR | CAT# 926-68070 |
| IRDye® 680RD Goat anti-Rabbit IgG Secondary Antibody | LI-COR | CAT# 926-68071 |
| Goat anti-Rabbit IgG (H+L) secondary, Alexa Fluor 488-conjugated | Invitrogen | CAT# A-11008 |
| Goat anti-Mouse IgG (H+L) secondary, Alexa Fluor 488-conjugated | Invitrogen | CAT# A-11001 |
| **Cell lines and tissue culture reagents** | | |
| THP-1 | ATCC | TIB-202 |
| HEK293T | ATCC | CRL-3216 |
| Human PBMC | Clinical partners | N/A |
| KOLF2.1S hiPSC | HipSci project | N/A |
| Flp-In T-REx 293 Cell Line | Invitrogen | R78007 |
| L-Glutamine (200 mM) | Gibco | 25030149 |
| Fetal Bovine Serum | Gibco | 10100147 |
| Poly-D-Lysine | Gibco | A3890401 |
| GlutaMAX Supplement | Gibco | 35050061 |
| β-Mercaptoethanol | Sigma-Aldrich | M6250 |
| RPMI-1640 Medium | Sigma-Aldrich | R0883 |

| | | |
|---|---|---|
| PMA/Phorbol 12-myristate 13-acetate | Sigma-Aldrich | P1585 |
| Penicillin-Streptomycin (10,000 U/mL) | Gibco | 15140122 |
| Zeocin | InvivoGen | ant-zn-1 |
| blasticidin | InvivoGen | ant-bl-1 |
| hygromycin B | InvivoGen | ant-hg-1 |
| Puromycin Dihydrochloride | Thermo Scientific | A1113803 |
| Dimethyl sulfoxide | Sigma-Aldrich | D8418 |
| Dulbecco's Phosphate Buffered Saline | Sigma-Aldrich | D8537 |
| **Chemicals, peptides, and recombinant proteins** | | |
| Suberic acid bis(N-hydroxysuccinimide ester) | Sigma-Aldrich | S1885 |
| Sodium deoxycholate | Sigma-Aldrich | D6750 |
| Ultrapure LPS, E. coli 0111:B4 | InvivoGen | tlrl-3pelps |
| Cycloheximide solution | Sigma-Aldrich | C4859-1ML |
| Bafilomycin A1 from Streptomyces griseus | InvivoGen | B1793 |
| 16% Formaldehyde (w/v), Methanol-free | Thermo Scientific | 28906 |
| PhosSTOP phosphatase inhibitor | Roche | 4906837001 |
| cOmplete™, Mini, EDTA-free Protease Inhibitor Cocktail | Roche | 11836170001 |
| Trichloroacetic acid | Sigma-Aldrich | T6399 |
| Pierce™ DTT (Dithiothreitol) | Thermo Scientific | 20290 |
| Iodoacetamide | Sigma-Aldrich | A3221 |
| Lipofectamine™ 3000 Transfection Reagent | Invitrogen | L3000001 |
| Lipofectamine™ 2000 Transfection Reagent | Invitrogen | 11668030 |
| Lipofectamine™ RNAiMAX Transfection Reagent | Invitrogen | 13778100 |
| Sequencing-grade modified trypsin | Promega | V5111 |
| Tween-20 | Sigma-Aldrich | P1379-1L |
| Triton X-100 | Sigma-Aldrich | T9284-500ML |
| Bromophenol blue | Sigma-Aldrich | B0126 |
| Biotin | Sigma-Aldrich | B4501 |
| PMSF | G-Biosciences | 786-055 |
| Hydrogen peroxide ($H_2O_2$), 30% (wt/wt) | Sigma-Aldrich | H1009-100ML |
| Trifluoroacetic acid | Sigma-Aldrich | 91707 |
| Formic acid | Sigma-Aldrich | 56302 |

| | | |
|---|---|---|
| Biotin-phenol | | |
| Dynabeads™ MyOne™ Streptavidin T1 | Invitrogen | 65602 |
| Sodium ascorbate | Sigma-Aldrich | A7631 |
| Trolox | Sigma-Aldrich | 238813-5G |
| Sodium azide | Sigma-Aldrich | S2002 |
| MG132, Ready Made Solution | Sigma-Aldrich | M7449-1ML |
| TCEP | Gold Biotechnology | TCEP2 |
| IGEPAL® CA-630 | Sigma-Aldrich | I8896 |
| Triton™ X-100 | Sigma-Aldrich | X100 |
| Nuclease-Free Water (not DEPC-Treated) | Invitrogen | AM9932 |
| Benzonase® Nuclease | Millipore | E1014 |
| **Biochemistry assays** | | |
| Caspase-Glo® 1 Inflammasome Assay | Promega | G9951 |
| Pierce™ BCA Protein Assay Kit | Thermo Scientific | 23225 |
| InstantBlue® Coomassie Protein Stain (ISB1L) | Abcam | ab119211 |
| CyQUANT™ LDH Cytotoxicity Assay | Invitrogen | C20300 |
| CellTiter 96® AQueous One Solution Cell Proliferation Assay (MTS) | Promega | G3582 |
| Dynabeads™ Co-Immunoprecipitation Kit | Invitrogen | 14321D |
| Human IL-1 beta/IL-1F2 DuoSet ELISA | R&D Systems | DY201 |
| Human IL-6 DuoSet ELISA | R&D Systems | DY206 |
| Human TNF-alpha DuoSet ELISA | R&D Systems | DY210 |
| LightCycler® 480 SYBR Green I Master | Roche | 04707516001 |
| High-Capacity cDNA Reverse Transcription Kit | Thermo Scientific | 4368814 |
| RNeasy Mini Kit | Qiagen | 74104 |
| Stop Solution 2N Sulfuric Acid | R&D Systems | DY994 |
| Recombinant DNA | | |
| pOG44 Plasmid Vector | ThermoFisher Scientific | CAT# V600520 |
| pcDNA5/FRT/TO GFP | Addgene | CAT# 19444 |
| pcDNA5/FRT/TO APEX2-NLRP3-Flag | Generated in this study (Backbone 19444) | N/A |
| pEGFP-C2-NLRP3 (ITEM 73955) | Addgene | N/A |
| pNLRP3 FLAG Full length | Generated in this study (Backbone 73955) | N/A |

| | | |
|---|---|---|
| pNLRP3 NACHT+ LRR- FLAG (140-1035) | Generated in this study (Backbone 73955) | N/A |
| pNLRP3 LRR only- FLAG (700-1035) | Generated in this study (Backbone 73955) | N/A |
| pNLRP3 Pyrin + NACHT- FLAG (1-700) | Generated in this study (Backbone 73955) | N/A |
| pNLRP3 NACHT only- FLAG (140 -700) | Generated in this study (Backbone 73955) | N/A |
| **Software and algorithms** | | |
| Prism | GraphPad, version 9 | https://www.graphpad.com/scientific-software/prism/ |
| Perseus | Nature methods 13.9 (2016): 731-740. Version 1.6.15.0 | https://maxquant.net/perseus/ |
| ImageStudioLite | LI-COR, version 5.2 | https://www.licor.com/bio/image-studio-lite/ |
| FiJi | Nature Methods, 9(7), 676–682. | https://imagej.net/software/fiji/ |
| Cytoscape | Genome Research 2003 Nov; 13(11):2498-504 | https://cytoscape.org/ |
| ZEN | Carl Zeiss | RRID: SCR_013672 |
| Illustrator | Adobe | https://www.adobe.com/uk/ |
| Photoshop | Adobe | https://www.adobe.com/uk/ |
| MaxQuant | Nat Protoc. 2016 Dec;11(12):2301-2319. Version v1.6.10.43 | http://www.maxquant.org |

587

588 **Method details**

589 **Cell culture**

590 THP-1 cells were cultured in 10% FBS (Gibco #10500-64) RPMI 1640 (Sigma) supplemented with 2%
591 L-glutamine (G7513, Sigma-Aldrich), 0.05 mM β-mercaptoethanol (Sigma), and antibiotics
592 (penicillin/streptomycin, Gibco). HEK293T cells were cultured in high glucose DMEM, supplemented
593 with 10% FBS, and 2% L-glutamine. Flp-In T-REx 293 cell line (R78007, ThermoFisher) were cultured
594 in high glucose DMEM, supplemented with 10% FBS, 2% L-glutamine, 100 µg/mL Zeocin (InvivoGen,
595 ant-zn-1) and 15 µg/mL blasticidin (InvivoGen, ant-bl-1) at 37 °C in a humidified 5% CO2 atmosphere.
596 The stably transfected Flp-In T-REx 293 cell lines (flag-NLRP3 and flag-NLRP3-APEX2) were
597 cultured in the same medium and selected by 100 µg/mL hygromycin B (InvivoGen, ant-hg-1). 1 µg/mL
598 tetracycline was added to induce the expression of flag-NLRP3 or flag-NLRP3-APEX2.

599 **PBMC isolation and *in vitro* culture**

600 To isolate the mononuclear cells, leukocyte cones (around 4 mL) were diluted in 25 mL RPMI medium
601 before laid onto 15 mL LymphoPrep without disturbing the interface between LymphoPrep and the
602 cone blood. Subsequently, it was centrifuged at 2000 rpm (400 g) at room temperature for 20 min.

603 Lymphocytes, which form a thin layer of white film after the centrifuge, are transferred into a fresh 50
604 mL tube with a Graduated Pasteur Pipette and washed twice with RPMI medium. PBMCs were plated
605 in 6-well plate at 1-2 × $10^7$ cells/mL in 10 mL and allowed to adhere at 37°C for 4 hrs. Non-adherent
606 cells were removed thorough washing with RPMI-1640.

607 **hiPSC culture and differentiation to microglia**

608 The KOLF2.1S hiPSC line used for this study was obtained with informed consent from all subjects,
609 donors and/or their legal guardian(s) and with the approval of all the relevant institutions. All methods
610 and experimental protocols were carried out in accordance with University of Oxford guidelines and
611 regulations. hiPSC lines were generated previously as part of the HipSci project (REC Reference
612 09/H0304/77, covered under HMDMC 14/013 and REC reference 14/LO/0345). KOLF2.1S was
613 generated from the parental KOLF2-C1 line (https://hpscreg.eu/cell-line/WTSIi018-B-1) itself a clonal
614 isolate of KOLF2 (https://hpscreg.eu/cell-line/WTSIi018-B) by correction of a heterozygous loss of
615 function mutation ARID2 using CRISPR based homology repair by the Cellular Operations Gene
616 Editing team at the Wellcome Sanger Institute (Bruntraeger et al., 2019). hiPSC were cultured in OxE8
617 medium with daily media changes (Vaughan-Jackson et al., 2021) on Geltrex (Gibco A1413302) coated
618 tissue culture dishes and passaged with 0.5mM EDTA. hiPSC were differentiated into microglial
619 precursors through the formation of embryoid bodies (EB) (van Wilgenburg et al., 2013) by seeding 4
620 x $10^6$ hiPSC per well of an Aggrewell 800 plate (STEMCELL Technologies, 34815) in EB medium
621 (OxE8 supplemented with 50 ng/mL BMP4 (PeproTech PHC9534), 50 ng/mL VEGF (PeproTech
622 PHC9394), and 20 ng/mL SCF (Miltenyi Biotec 130-096-695)). After differentiating in EB media for
623 6 days (with daily 50% media changes), 150 EB were transferred to T175 coated with 0.1% Gelatin
624 containing differentiation media (X-VIVO 15 (Lonza BE02-060F), 1x GlutaMAX (Lifetech 25050-
625 061), 50µM β-mercaptoethanol (LifeTech 31350-010), 100 ng/mL M-CSF (Gibco, PHC9501), 25
626 ng/mL IL-3 (Gibco, PHC0033). After 4-5 weeks of differentiation, microglial precursors shed into the
627 media are harvested weekly by collection of supernatant and pelleting at 400 x g for 5 minutes.
628 Microglial precursors are then resuspended in the final microglia maturation media ITMG
629 (ADMEM/F12 (LifeTech, 12634-010), 1x GlutaMAX (Lifetech, 25050-061), 100 ng/mL IL-34
630 (PeproTech, 200-34-500), 50 ng/mL TGFβ-1 (PeproTech, 100-21C-250), 25 ng/mL M-CSF (Gibco,
631 PHC0033), 10 ng/mL GM-CSF (Gibco, PHC2013), as previously described (Washer et al., 2022), and
632 differentiated to hiPSC-microglia for 14 days, with 50% media changes every 3 to 4 days. All
633 differentiation steps are carried out at 37°C, 5% CO2.

634 **Inflammasome activation assay**

635 THP-1 cells were plated in a concentration of 1x$10^6$ cells/mL and incubated with 0.5 µM PMA for 4 h.
636 After differentiation, PMA-containing media was replaced with fresh media. Experiments were carried
637 out on the following day. Differentiated THP-1 cells were primed with LPS (1 µg/mL) for 4 h, followed

638 by the treatment of PBS (mock) or 5 μM nigericin for 45 min. After stimulation, supernatants and cell
639 lysates were collected separately, or combined together for immunoblotting analysis.

640 **ASC speck oligomer crosslinking**

641 PMA-differentiated THP-1 cells were primed with LPS (1 μg/mL) for 4 h, and then stimulated with
642 nigericin (10μM) for 45 min. Cells were lysed on ice in Buffer A (20 mM HEPES-KOH, pH 7.5, 10
643 mM KCl, 1.5 mM $MgCl_2$, 1 mM EDTA, 1 mM EGTA, 320 mM sucrose, and protease inhibitor cocktail),
644 and homogenized using a 21-gauge needle. The lysates were centrifuged at 1,800 rpm (300 g) for 8 min
645 at 4 °C. Supernatants were transferred to a new tube and diluted with 1 volume of CHAPS buffer (20
646 mM HEPES-KOH, pH 7.5, 5 mM MgCl2, 0.5 mM EGTA, 0.1% CHAPS, and protease inhibitor
647 cocktail). The diluted lysates were then centrifuged at 5,000 rpm (2,400 g) provide g for 8 min to obtain
648 the crude inflammasome-containing pellets. The pellets were washed with ice cold PBS twice,
649 resuspended in CHAPS buffer, and then cross-linked at 37 °C for 20 min by adding 2mM DSS
650 (disuccinimidyl suberate, dissolved in DMSO). The reaction was quenched by adding SDS sample
651 buffer and followed by Western blotting analysis.

652 **Enzyme-linked immunosorbent assay (ELISA)**

653 Human IL-1β (DY201, R&D Systems) and IL-6 (DY206, R&D Systems) production in the supernatants
654 were detected by ELISA kit according to manufacturer's protocol. Plates were coated with diluted
655 capture antibody in sterile PBS at room temperature overnight. On the following day, plates were
656 washed three times with 200 μL/well wash buffer (0.05% Tween 20 in PBS, pH 7.2-7.4) before being
657 blocked with 200 μL/well reagent diluent (1% BSA in PBS, pH 7.2-7.4, 0.2 μm filtered) at room
658 temperature for a minimum of 1 h. After blocking, plates were washed three times and incubated with
659 samples or standards (in reagent diluent) for 2 h at room temperature. After three washes of plates, 100
660 μL/well detection antibody (diluted in reagent diluent) was added to the wells and incubated for 2 h at
661 room temperature. Plates were then washed three times and incubated with 100 μL/well Streptavidin-
662 HRP for 20 min at room temperature, followed by another three washes and incubation with 100
663 μL/well substrate solution (1:1 mixture of Colour Reagent A ($H_2O_2$) and Colour Reagent B
664 (Tetramethylbenzidine)) at room temperature. 20 min after the reaction, 50 μL/well stop solution (2 N
665 H2SO4, DY994, R&D Systems) was added and mixed thoroughly to quench the reaction. The optical
666 density of each well was determined at the wavelength of 450nm, and the relative concentration was
667 calculated based on the standard curve, generated through a 3 parameter logistic curve fit using the data
668 from standard samples.

669 **TCA/DOC protein precipitation**

670 Trichloroacetic acid (TCA)- deoxycholate (DOC) precipitation was commonly used to concentrate the
671 proteins in supernatants and this method was adapted from André et al. Briefly, 8.5 μL of 2% Na-

672 deoxycholate was added to 1 mL sample with a final concentration of 125 μg/mL. This mixture was
673 incubated at room temperature for 15 min and 333 μL of 24% TCA (final concentration 6%) was added
674 to the samples. Proteins were precipitated and centrifuged at 12,000 g for 30 min at 4°C. Supernatant
675 was carefully removed and the pellets were washed once with acetone to remove excessive TCA before
676 another centrifuge at 12,000 g for 5 min. After removing the supernatants, the resulting pellets were
677 solubilised in loading buffer and subjected to immunoblotting analysis.

678 **Cytotoxicity and cell viability assay**

679 Relevant cells were treated as indicated, and the cytotoxicity was detected using CyQUANT™ LDH
680 Cytotoxicity Assay (Invitrogen) according to manufacturer's instruction. Briefly, 50 μL of each sample
681 supernatant was transferred to 96-well flat-bottom plate in triplicate wells, and then, 50 μL of premixed
682 reaction buffer was added to each well. The plate was incubated for 30 min at room temperature before
683 addition of 50 μL/well stop solution. The optical density of each well was measured at the wavelength
684 of 490nm and 680nm (680 nm absorbance was used as background), and the cytotoxicity (% LDH
685 release) was calculated according to manufacturer's protocol.

686 Cell viability was measured using CellTiter 96 AQueous One Solution Cell Proliferation Assay (MTS,
687 Promega). Briefly, 20μl of CellTiter 96® AQueous One Solution Reagent was added to each well
688 containing samples in 100 μl of culture medium. The plate was then incubated for a minimum of 1h at
689 37°C. The absorbance of each well was measured at the wavelength of 490nm, and the cell viability
690 was calculated according to manufacturer's protocol.

691 **Caspase-1 activity bioluminescent assay**

692 Relevant cells were treated as indicated, and the caspase-1 activity in the culture medium (supernatant)
693 was measured using Caspase-Glo® 1 Inflammasome Assay (Promega) according to manufacturer's
694 instruction. Briefly, Caspase-Glo 1 Reagent was prepared through resuspension of Z-WEHD substrate
695 using Caspase-Glo 1 buffer, and the addition of MG132 inhibitor to a final concentration of 60 μM.
696 Afterwards, 50 μL of cell culture medium was transferred to the 96-well plate, followed by adding 5
697 μL Caspase-Glo 1 Reagent. The contents of the wells were thoroughly mixed and incubated at room
698 temperature for at least 1 hour for the signal to be stable. Subsequently, the luminescence value was
699 measured using multi-mode microplate reader FLUOstar Omega (BMG LABTECH) according to
700 manufacturer's instruction.

701 **Immunoprecipitation**

702 Cells were washed with ice-cold PBS for two times, and then lysed in Pierce® IP lysis buffer (25 mM
703 Tris-HCl pH 7.4, 150 mM NaCl, 1% NP-40, 1 mM EDTA, 5% glycerol, PhosSTOP phosphatase
704 inhibitor and cOmplete™ Protease Inhibitor Cocktail). Lysates were incubated on ice for 10 min with
705 periodic mixing, and then clarified at 13,000 g for 10 min at 4°C to remove the cell debris. Pre-cleared

706 lysates were incubated with anti-FLAG® M2 Magnetic Beads at room temperature for 30 min. After
707 three times of washes with TBS, the proteins bound by the anti-flag antibody were pulled down and 3X
708 FLAG® peptide was added for elution. Both the whole cell lysates and the pull-down samples are
709 subjected to immunoblotting analysis.

710 **Transient transfection**

711 For DNA plasmids: Cells were grown in 6-well plates and Lipofectamine 3000 Transfection Reagent
712 (L3000001, ThermoFisher UK) was used to transfect the cells following the manufacturer's instructions.
713 The concentration of plasmids used was indicated in each experiment. For siRNA transfection
714 experiments: Cells were grown in 6-well plates and RNAimax transfection reagent (Invitrogen, 13778-
715 150) was used following the manufacturer's protocol. A final concentration of 10 nM of the following
716 Silencer™ select siRNAs were used: control siRNA (4390844), si-NLRP3 (s41554) and si-UCH-L1
717 (s14616).

718 **Construction of plasmids**

719 The full list and descriptions of all primers and plasmids used in this study can be found in key resources
720 table. For the generation of NLRP3-APEX2, NLRP3-Flag, NEBuilder HiFi DNA Assembly (NEB:
721 E5520S) was used following manufacture protocol. Primers were designed using the NEBuilder
722 Assembly Tool. The successful clones were confirmed using both PCR and DNA sequencing. Finally,
723 the expression plasmids for NLRP3 domains were generated using the Q5® Site-Directed Mutagenesis
724 Kit (NEB: E0554S) following manufacture protocols. We used as a template the GFP- NLRP3 plasmid
725 (Addgene), we initially replace GFP with Flag. Finally, different domains were deleted to generate the
726 successful plasmids. The successful clones were confirmed using both PCR and DNA sequencing.

727 **Generation of stable cell line**

728 The Flp-In T-Rex 293 stable cell lines (flag-NLRP3 and flag-NLRP3-APEX2) were generated using
729 Lipofectamine 3000 following manufacture protocol in a 6-well plate. The cells were transfected with
730 both the expression plasmid and the plasmid pOG44 in a ratio of 1:9. Cells were split the following day
731 and transferred in a 100mm dish. After 8 hours, 300 µg/mL hygromycin B was added into the medium
732 for selection.

733 **sgRNA design, lentivirus production and transduction**

734 Non-targeting control (NTC) and UCH-L1-targeting sgRNA sequences were designed using CRISPick
735 tool (https://portals.broadinstitute.org/gppx/crispick/public). To clone the target sequences into the
736 lentiCRISPRv2 backbone (one vector system), two oligos containing the target sequences were
737 synthesized (Sigma) and inserted into the digested lentiviral construct. sgRNA sequences are as
738 followed: UCH-L1-sgRNA#1: 5'-ACTTCATGAAGCAGACCATT-3'; UCH-L1-sgRNA#2: 5'-

739 AATCGGACTTATTCACGCAG-3'; UCH-L1-sgRNA#3: 5'- AAGACAAACTGGGATTTGGT-3'.
740 HEK293T cell lines were seeded at 40% confluency and transfected with pMD2G, psPAX2 and the
741 above lentiCRISPRv2 plasmids using lipofectamine 2000 following manufacturer's instructions. After
742 incubation for two days, supernatants were collected and filtered by 0.45μm filter, followed by
743 ultracentrifuge to obtain concentrated viral particles.

744 **Biotin-phenol proximity labelling and biotinylated proteins capture**

745 This method was adapted from that previously reported by Stephanie et al. $5\times10^6$ Flp-In T-Rex HEK293
746 stable cells were induced with 1 μg/mL tetracycline overnight. The next day cells were incubated with
747 medium containing 500 μM biotin-phenol (BP) for 30 min at 37 °C under 5% CO2. Afterwards, a final
748 concentration of 1 mM $H_2O_2$ was added and incubated for 40 seconds. The reaction was then quenched
749 by the addition of quenching buffer (10mM sodium ascorbate, 10mM sodium azide, 5mM Trolox in
750 DPBS). Subsequently, cells were washed with quenching buffer for three times, PBS for two times and
751 then lysed with RIPA lysis buffer containing 1 mM PMSF, 5 mM Trolox, 10 mM sodium azide, 10 mM
752 sodium ascorbate, PhosSTOP phosphatase inhibitor and cOmplete™ Protease Inhibitor Cocktail.
753 Samples were then briefly sonicated and centrifuged at 10,000 g for 10 min at 4°C to remove cell debris.
754 For streptavidin pull-down experiments, Dynabeads MyOne Streptavidin T1 was prepared and washed
755 with RIPA lysis buffer twice. The cleared lysate was applied to the magnetic beads and at RT for 1 hour.
756 Afterwards, the beads were washed for two times with RIPA lysis buffer, once with 1M KCL, 0.1 M
757 $Na_2CO_3$ and 2 M Urea (in 10 mM Tris-HCL, pH 8) and finally twice with RIPA buffer again. For
758 western blot analysis, biotinylated proteins were eluted using 60 μL of 3×loading buffer supplemented
759 with 2 mM biotin and 20 mM DTT by boiling (98°C) for 10 min. For Mass spectrometry analysis, an
760 on-beads digestion protocol was used as described below. Samples were denatured in 8 M Urea (in 100
761 mM triethylammonium bicarbonate buffer (TEAB)) and incubated at room temperature for 30 min.
762 Afterwards, the samples were reduced with 10mM tris(2-carboxyethyl)phosphine (TCEP) for at room
763 temperature 30 min. Samples were alkylated by the addition of iodoacetamide (final concentration 50
764 mM) and incubated at room temperature for 30 min. The reaction was quenched by adding DTT (final
765 concentration 20 mM), and the urea concentration were diluted down to 1.5 M by adding TEAB.
766 Biotinylated proteins were digested through the incubation with trypsin (1 μg trypsin per 20 μL
767 streptavidin beads) overnight at 37 °C. Following the trypsinization, samples were desalted using the
768 C18 solid phase cartridge (Sep-Pak, Waters) according to the manufacturer's protocol. Purified peptide
769 eluates were dried down in the speed-vac, re-suspended in buffer A (98 % MilliQ-H20, 2 % $CH_3CN$
770 and 0.1 % trifluoroacetic acid - TFA) and stored at -20 °C until further analysis.

771 **Affinity-purification mass spectrometry (AP-MS)**

772 $1\times10^7$ HEK293 FLAG-NLRP3 Flp-In T-Rex stable cells were induced with 1 μg/mL tetracycline
773 overnight. The next day cells were incubated with medium with Nigericin (10μM) or DMSO for 90 min

774 at 37 °C under 5% $CO_2$. Cells were washed with ice-cold PBS for five times, and then lysed in Pierce
775 IP lysis buffer (25 mM Tris-HCl pH 7.4, 150 mM NaCl, 1% NP-40, 1 mM EDTA, 5% glycerol,
776 PhosSTOP phosphatase inhibitor and cOmplete™ Protease Inhibitor Cocktail). Lysates were incubated
777 on ice for 10 min with periodic mixing, and then clarified at 13,000 g for 10 min at 4°C to remove the
778 cell debris. Pre-cleared lysates were incubated with anti-FLAG M2 Magnetic Beads at 4ºC overnight.
779 The next day beads were washed 3 times with TBS. Samples were eluted were eluted using 100 µL of
780 3×loading buffer supplemented 20 mM DTT by boiling (98°C) for 10 min.
781

782 **Mass spectrometry analysis**

783 An Orbitrap Fusion Lumos Tribid mass spectrometer (Thermo Fisher Scientific) coupled to an Ultimate
784 3000 UHPLC (Thermo Fischer Scientific) platform was used to analyse the purified tryptic peptides by
785 liquid chromatography tandem mass spectrometry (LC-MS/MS) as described previously (Davis et al.,
786 2017). In brief, ten per cent of tryptic peptides (~ 200 ng) were loaded onto a trap column (PepMapC18;
787 300µm x 5mm, 5µm particle size, Thermo Fischer) and separated on a 50 cm EasySpray column
788 (ES803, Thermo Fischer) using a 60 minute linear gradient ranging from 2 % to 35% buffer B (A: 5%
789 DMSO, 0.1% formic acid; B: 5% DMSO, 0.1% formic acid in acetonitrile) at a flow rate of ~250
790 nL/min. Eluted peptides were then subjected to electrospray ionisation (ESI) and directed into an
791 Orbitrap Fusion Lumos Tribrid mass spectrometer (instrument control software v3.3). Data were
792 acquired in data-dependent mode (DDA), with the advance peak detection (APD) feature enabled.
793 Survey scans were acquired in the Orbitrap at 120 k resolution over a m/z range 400 -1500, AGC target
794 of 4e5 and S-lens RF of 30. Fragment ion spectra (MS/MS) were obtained in the Ion trap (rapid scan
795 mode) with a Quad isolation window of 1.6, 40% AGC target and a maximum injection time of 35 ms,
796 with HCD activation and 28% collision energy. Raw MS files were analysed using MaxQuant software
797 (v1.6.10.43) using label free quantitation (LFQ) as described previously (Olie et al., 2023). In brief, raw
798 MS files were searched against the UniProtKB human sequence database (UP000005640, 79,038
799 human sequence entries). The following parameters were set to perform label free quantification:
800 Modifications were set on Carbamidomethyl (C) as fixed and Oxidation (M) and Deamidation (NQ) as
801 variable and a maximum of two missed cleavages were allowed. Match between runs function was
802 used.

803 **RNA extraction and real time reverse transcription (RT)-PCR**

804 Total RNA was isolated with the TRIzol reagent (SigmaAldrich) according to the manufacturer's
805 instructions. The nucleic acid concentration was measured with the NanoDrop2000 (NanoDrop
806 Technologies, Inc.). Complementary DNA (cDNA) was synthesized from 1.5 µg of total RNA with the
807 High-Capacity cDNA Reverse Transcription Kit (Applied Biosystems, USA). Quantitative real-time
808 polymerase chain reaction (RT-qPCR) was performed using the LightCycler 480 SYBR Green I Master

809 kit and LightCycler 480 PCR System (Roche, Switzerland) according to the manufacturer's instructions.
810 The Delta-Ct method was used to calculate the relative RNA expression levels.
811

812 **Pathway enrichment analysis**

813 Filtered proximity proteomes (SAINT probability > 0.8, FC-A ≥ 1) either in DMSO control or nigericin
814 activated samples were imported into the STRING database search portal (version 11.5, Szklarczyk et
815 al., 2021; von Mering et al., 2003), and the top 20 retrieved terms were plotted with both strength (Log10
816 [observed / expected]) and false discovery rate (FDR) (interaction score ≥ 0.7). Terms were clustered
817 through the similarity of enrichment strength patterns across the four groups and the results were further
818 visualized using clusterProfiler 4.0 (Wu et al., 2021; Yu et al., 2012).

819 **PPIs network construction**

820 Differentially enriched proteins under unstimulated or stimulated condition that passed the filtering
821 criteria (log2[FC]≥0.5 or ≤-0.5, FDR≤ 0.05) were separately uploaded to the STRING portal, and
822 physical subnetwork type was chosen to extract the physical (direct) protein-protein associations from
823 the databases. Active interaction sources, including text mining, experiments, and databases, and an
824 interaction score > 0.7 (high confidence interaction) were applied to construct the PPI networks.
825 Markov clustering algorithm (MCL) was used to group the interaction subnetworks with the inflation
826 value of 3.0, resulting in 13 clusters for the stimulated condition and 18 clusters for the unstimulated
827 condition.

828 **SAINT probabilistic scoring for NLRP3 APEX2 PL-MS and AP-MS data**

829 The computational tool, SAINTexpress (Teo et al., 2014)- an updated version of the "Significance
830 Analysis of INTeractome (SAINT)," was utilised to allocate confidence scores to the proximity
831 labelling and AP-MS data. This analysis was conducted via the online Contaminant Repository for
832 Affinity Purification platform at www.crapome.org (Mellacheruvu et al., 2013).

833 **Statistics and reproducibility**

834 Data are presented as mean ± standard error of the mean (SEM). Two-tailed, unpaired student's t test
835 was used for statistical analysis in GraphPad Prism 9. Unless stated, otherwise all quantitative
836 experiments were performed in triplicates and average with SEM reported.

837 **Data availability**

838 The mass spectrometry proteomics data have been deposited to the ProteomeXchange Consortium via
839 the PRIDE (Deutsch et al., 2023; Perez-Riverol et al., 2022) partner repository with the dataset identifier
840 PXD045862.

841 **Acknowledgements**

842 Z.L., A.D., I.V., G.L., X.Z., R.F., T.D. and B.M.K. were supported by the Chinese Academy of Medical
843 Sciences (CAMS) Innovation Fund for Medical Science (CIFMS), China (grant number: 2018-I2M-2-
844 002) awarded to B.M.K., R.F. and T.D. B.M.K. was supported by Pfizer. E.D. was supported by
845 Alzheimer's Research UK Grants ARUK2015DDI-OX. E.J was funded by Wellcome Trust (grant #
846 224040/Z/21/Z). Imaging was performed using the Oxford-Zeiss Centre of Excellent in Biomedical
847 Imaging and the Kennedy Trust for Rheumatology Research (grant # 202117 and 202103, respectively).
848 E.W.T. was supported by a CRUK Programme Award (DRCNPG-Nov21\100001) with support from
849 the Engineering & Physical Sciences Research Council. We would also like to thank members of the
850 Discovery Proteomics Facility, the Kessler, Oxford Drug Discovery Institute groups for constructive
851 discussions and Raphael Heilig for his expert help with mass spectrometry.

852 **Author contributions**

853 B.M.K., E.D. and Z.L. designed the research and wrote the manuscript. Z.L. and A.D. performed the
854 NLRP3-APEX2 proximity labelling experiments and analysed the mass spectrometry data. Z.L. and
855 A.D. performed the DUB siRNA library screen experiment. I.V. operated mass spectrometer for LC-
856 MS/MS acquisition of the samples and contributed to data processing. E.J. performed confocal imaging
857 and analysis. S.J.W. and A.D. contributed to the culture of hiPSC and differentiated them into microglial
858 cells. E.W.T. and F.C. contributed to UCH-L1 inhibitor provision and study design. Z.L., A.D., I.V.,
859 E.J., F.H.L., S.J.W., G.L., G.Y., H.L., F.C., X.Z., R.F., T.D., E.W.T., E.D. and B.M.K discussed the
860 results, commented, and provided critical reviews on the manuscript.

861 **Competing interests**

862 E.W.T. is a founder and shareholder in Myricx Pharma Ltd, and receives consultancy or research
863 funding from Kura Oncology, Pfizer Ltd, Samsara Therapeutics, Myricx Pharma Ltd, MSD, Exscientia
864 and Daiichi Sankyo. The other authors declare no competing interests.

865

866

867

868

869

870

871

872 **Figure S1**

873

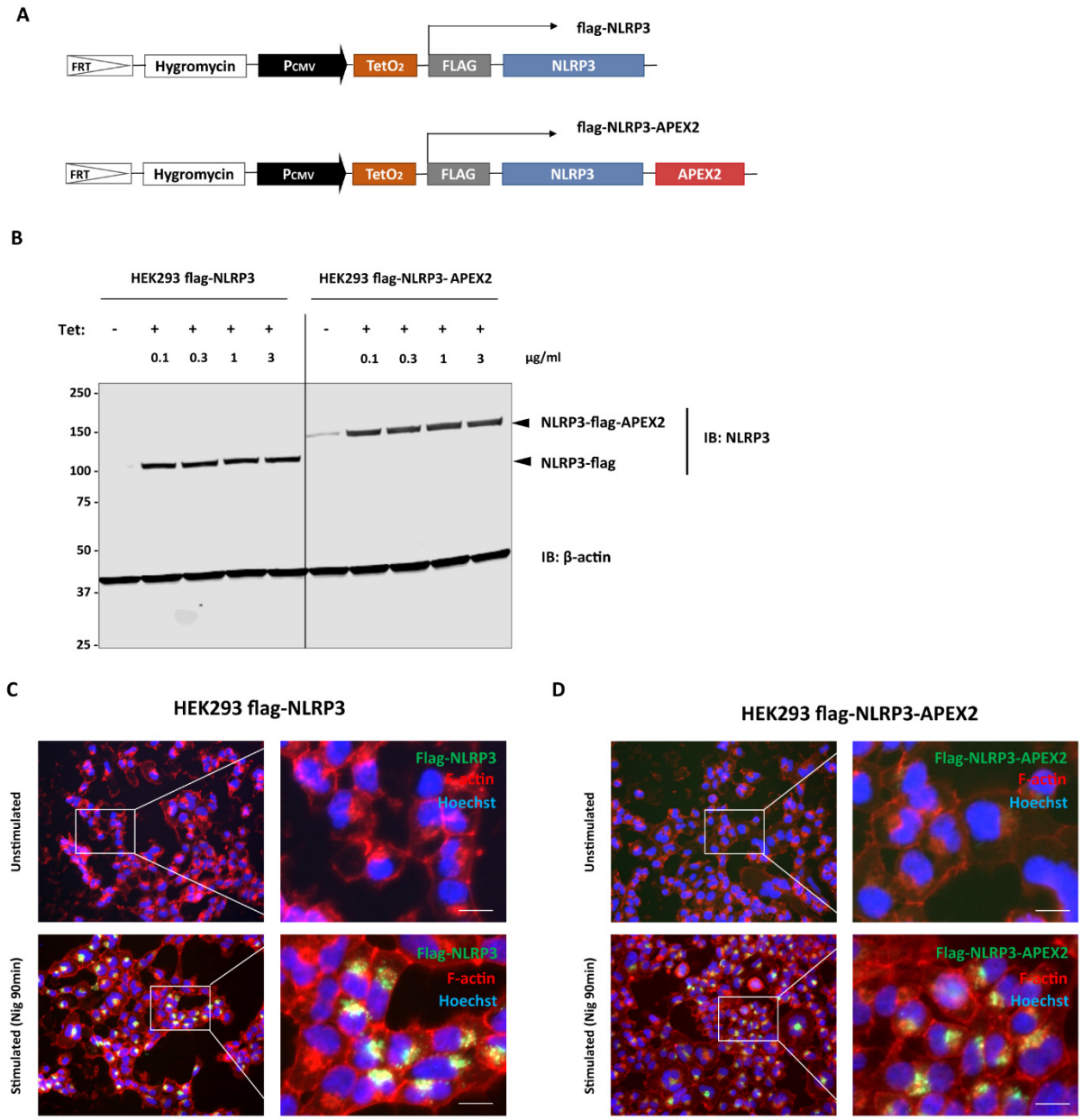


874

875 **Figure S1 | Construction of flag-NLRP3 and flag-NLRP3-APEX2 HEK293 stable cell line**

876 (A) Schematic of Flag-NLRP3 and Flag-NLRP3-APEX2 constructs. (B) Both the flag-NLRP3 and flag-
877 NLRP3-APEX2 Flp-In T-Rex HEK293 stable cell lines were treated with tetracycline at indicated
878 concentrations (0.1-3 μg/mL). 24 hours after induction, cell lysates were collected for immunoblotting
879 analysis. (C-D) Immunofluorescence of flag-NLRP3 (C) and flag-NLRP3-APEX2 (D) in Flp-In T-Rex
880 HEK293 stable cell lines. Cells were either treated with DMSO or Nigericin (10μM) for 90 min. Scale
881 bars, 10 μm.

882

883 **Figure S2**

884

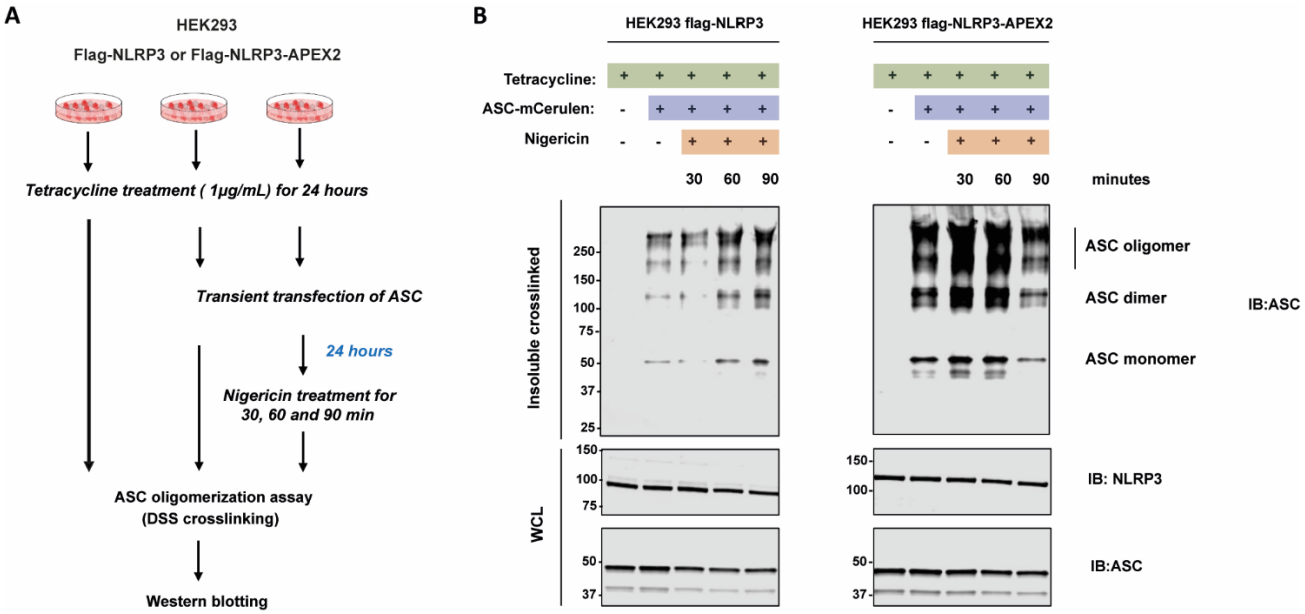


885

886 **Figure S2 | Reconstituted NLRP3 induces ASC oligomerization in HEK293 cell lines**

887 (A) Schematic of the ASC oligomerization assay in Flp-In T-Rex HEK293 stable cell lines. (B)
888 Immunoblot of DSS-crosslinked ASC oligomers in the lysates from flag-NLRP3 and flag-NLRP3-
889 APEX2 HEK293 stable cell lines, treated with tetracycline overnight, transfected with ASC mCerulean,
890 and followed by the treatment with nigericin (10µM) for the indicated time.

891
892
893
894
895
896
897
898
899
900
901
902
903
904
905
906
907

**Figure S3**

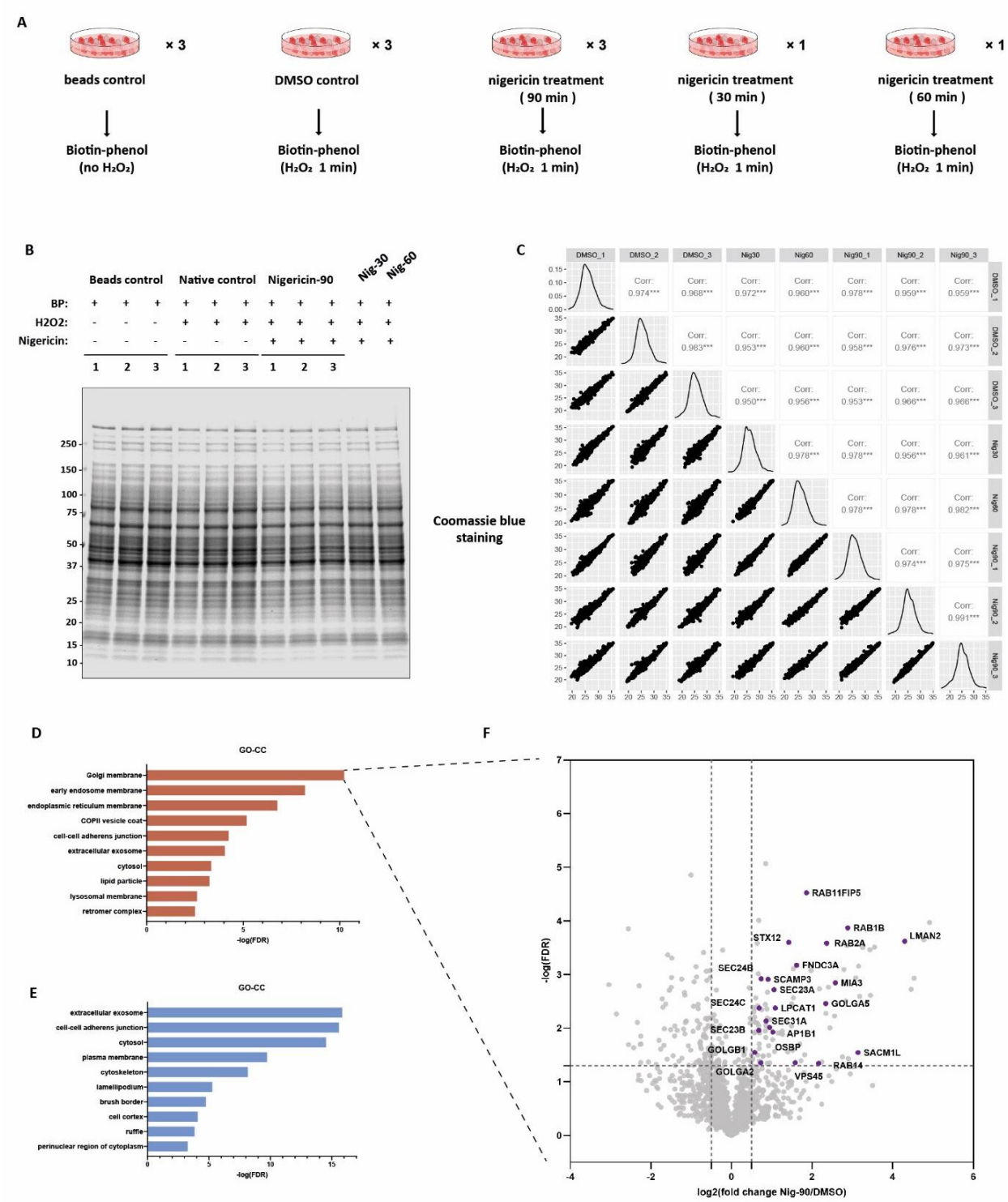


**Figure S3 | Tracing NLRP3 translocation using NLRP3-APEX2 proximity labelling**

(A) Scheme of the experimental design and procedures of NLRP3-APEX2 proximity labelling. (B) Coomassie blue staining of whole-cell lysates from HEK293 Flp-In T-Rex NLRP3-APEX2 cells, treated as indicated with tetracycline, biotin-phenol, $H_2O_2$, and nigericin. (C) Pearson correlation matrix heatmap of the biotinylated proteome profiling. This analysis confirms high reproducibility in protein

relative abundance measurements. (D-F) Bar graph showing the top 10 gene ontology-cellular component (GO-CC) terms of the proteins enriched in nigericin-stimulated state (nigericin treatment for 90 min) (D) and unstimulated state (DMSO treatment for 90 min) (E) respectively. (F) The 24 protein that belong to the Golgi membranes term are shown and coloured as purple in the volcano plotting.

942 **Figure S4**

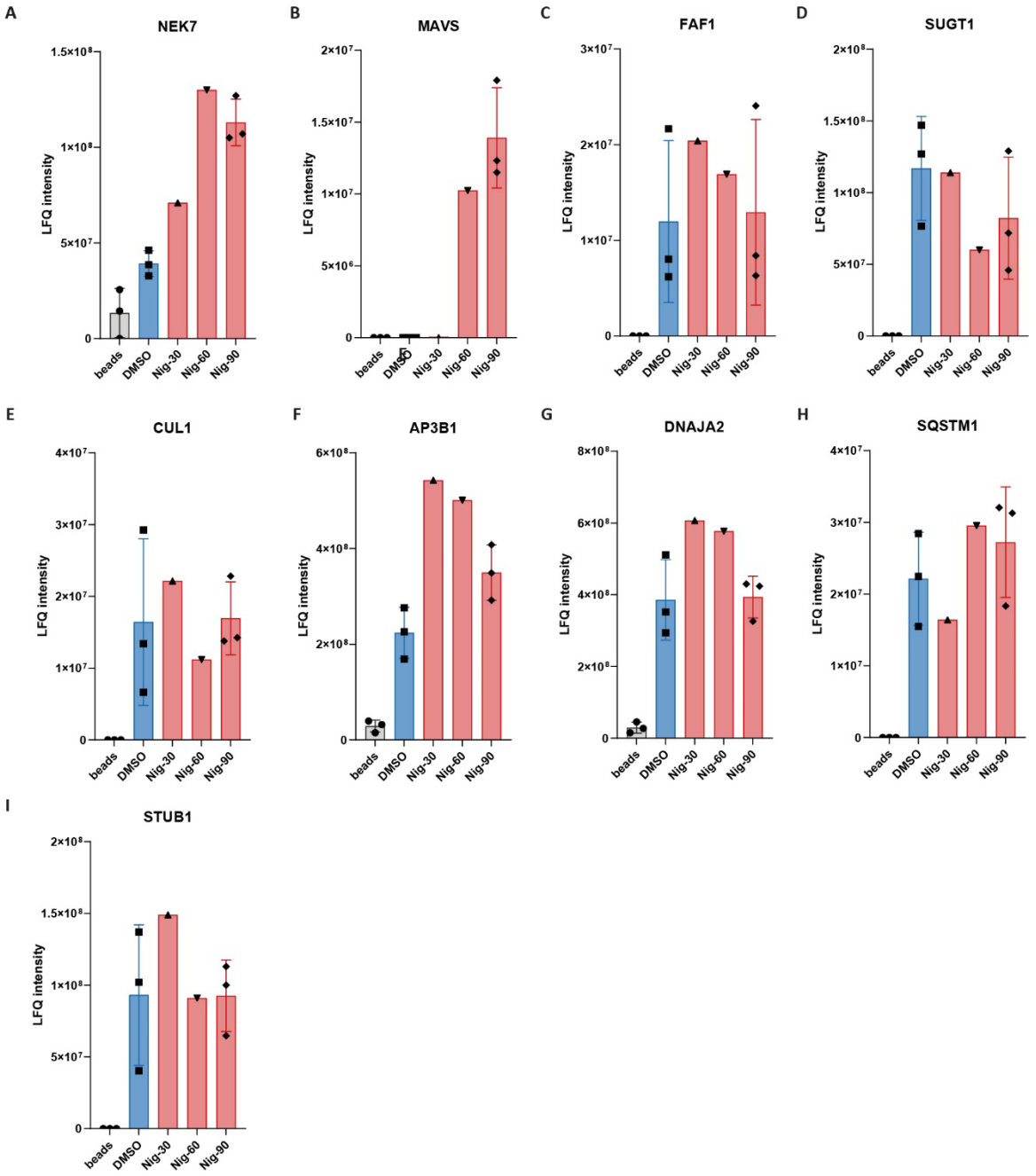


943

944 **Figure S4 | APEX2 proximity labelling identifies known NLRP3-interacting proteins during**
945 **NLRP3 activation downstream of potassium efflux**

946 (A-I) The raw LFQ Intensity values of the APEX2 NLRP3 proximity labelling from all the known
947 NLRP3-interacting proteins identified in our experiment. An average value of 3 independent
948 experiments is presented for DMSO and Nig-90 whereas for Nig-30 and Nig-60 just a single experiment.
949 Error bars show the standard deviation of the mean.

950

951

952 **Figure S5**

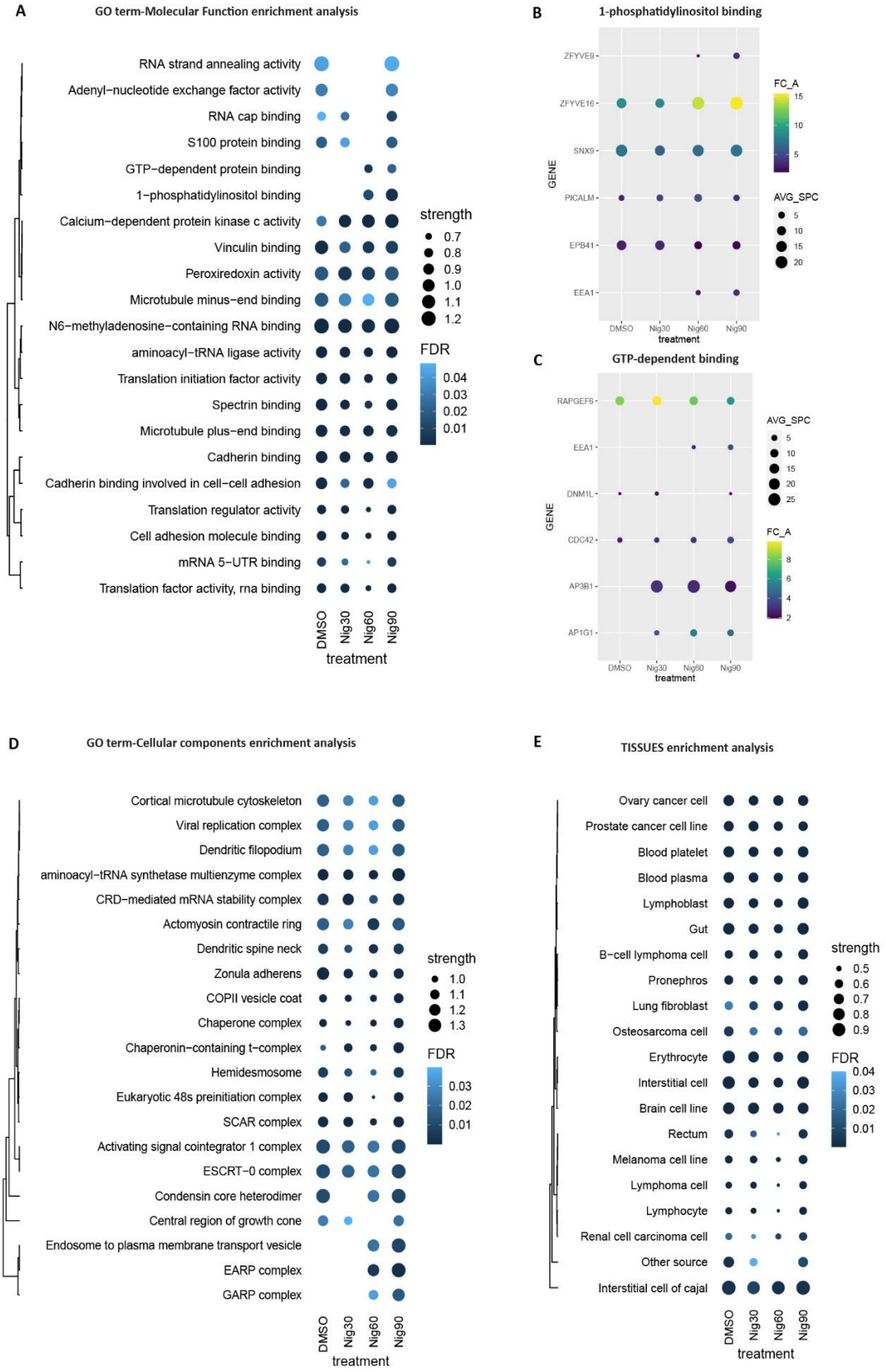


953

954 **Figure S5 | Functional analysis of the NLRP3 proximal proteins during inflammasome activation**

(A, D, E) Dot plots displaying the GOBP (A), GOCC (D) and TISSUE (E) enrichment analysis of high confidence NLRP3 proximal proteins upon nigericin stimulation for different timepoints as indicated. (B, C) Dot plots showing the average spectral counts (AVG_SPC) and fold change (FC_A) of NLRP3 proximal proteins enriched in the GOMF term 1-phosphatidylinostol binding (B) and GTP-dependent binding (C) respectively.

982 **Figure S6**

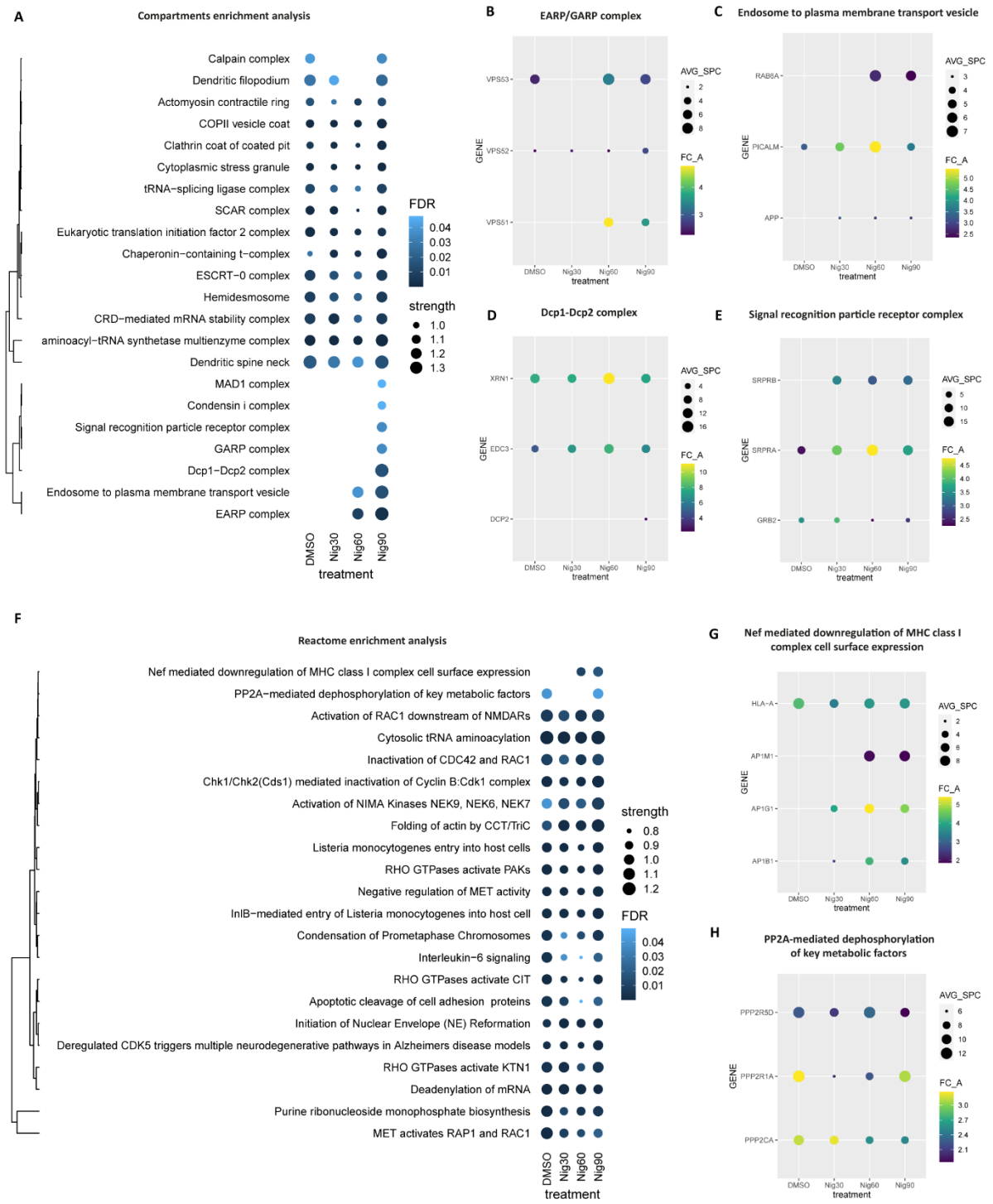


983

984 **Figure S6 | Functional analysis of the NLRP3 proximal proteins during inflammasome activation**
985 (A, D) Dot plots displaying the Compartments (A) and Reactome (F) enrichment analysis of high
986 confidence NLRP3 proximal proteins upon nigericin stimulation for different timepoints. (B-E, G-H)
987 Dot plots showing the average spectral counts (AVG_SPC) and fold change (FC_A) of NLRP3
988 proximal proteins enriched in the term EARP/GARP complex (B), Endosome to plasma membrane
989 transport vesicle (C), Dcp1-Dcp2 complex (D) and Signal recognition particle receptor complex (E),

990 Nef mediated downregulation of MHC class I complex cell surface expression (G), PP2A-mediated
991 dephosphorylation of key metabolic factors (H) respectively.
992
993
994
995
996
997
998
999
1000
1001
1002
1003
1004
1005
1006
1007
1008
1009
1010
1011
1012
1013
1014
1015

1016 **Figure S7**

1017

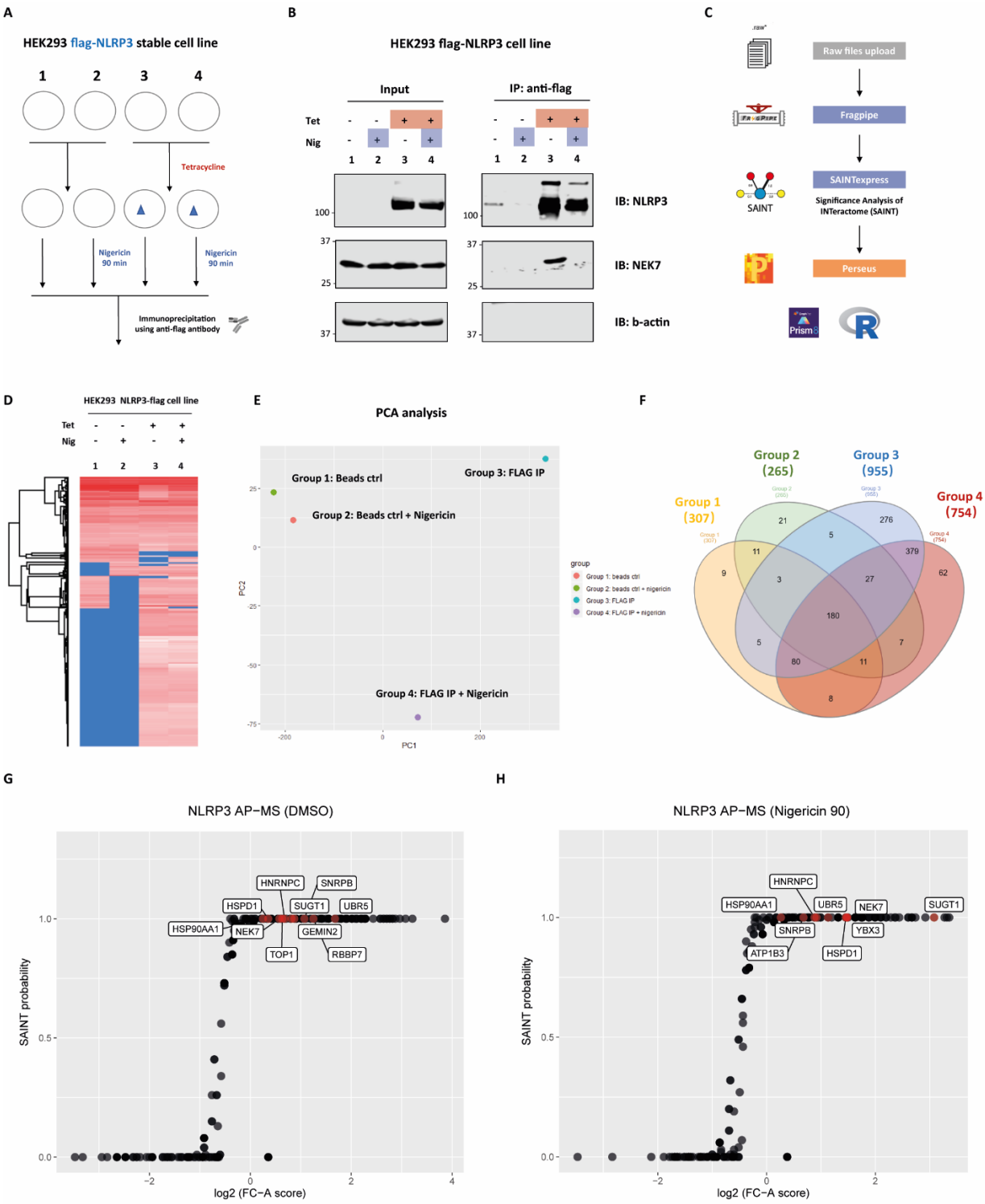


1018

1019

1020 **Figure S7 | NLRP3 interactome determined by AP-MS**

1021 (A) Schematic of the NLRP3 AP-MS experiment design. (B) Stable HEK293 cells expressing Flag-
1022 NLRP3 were incubated with tetracycline overnight. Subsequently, they were treated with nigericin for
1023 90 min as specified. NLRP3-flag was then isolated using an anti-flag antibody and subjected to

immunoblotting with the indicated antibodies. (C) Diagram illustrating the data analysis workflow for AP-MS data. (D) Heatmap showing the hierarchical clusters of prey proteins in the NLRP3 AP-MS across the four groups. (E) Principal component analysis of the four samples. Each dot represents an individual sample. (F) Venn diagram illustrating the number of proteins identified from different groups as indicated in (A). (G-H) SAINT probability scoring of the proteomic data for NLRP3 AP-MS compared to the negative beads control. Proteins passing the cut-off (SAINT probability ≥ 0.8, FC-A ≥ 1) are considered as high-confidence interacting proteins for NLRP3.

1061 **Figure S8**

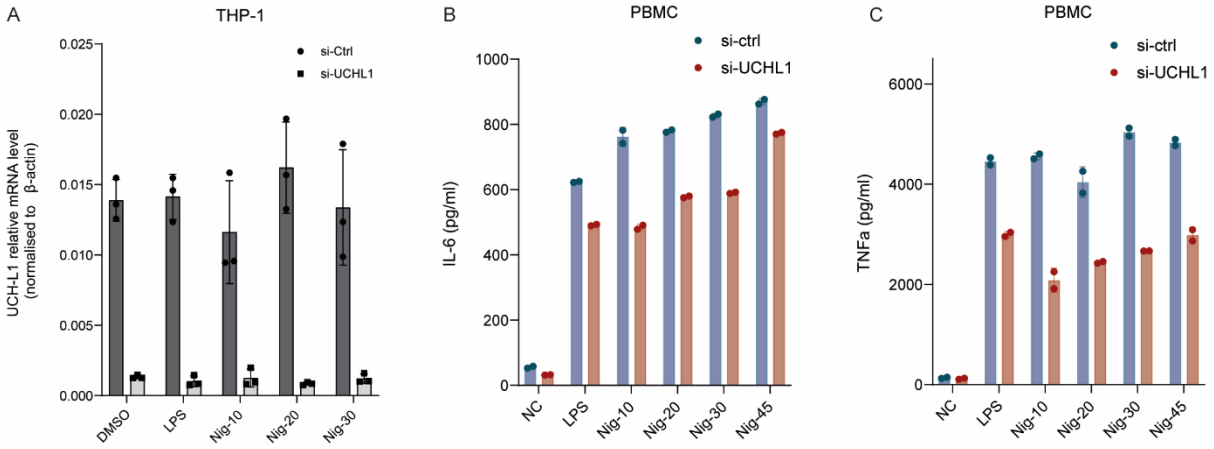


1062

1063 **Figure S8 | UCH-L1 deficiency decreases IL-6 and TNFα expression in human PBMC**

1064 (A) RT-qPCR analysis of UCH-L1 expression in THP-1 cells after transfection with either non-targeting
1065 siRNA or UCH-L1-targeted siRNA. Following differentiation with PMA, cells were primed using LPS
1066 (1 μg/mL) for 4 hours, and then treated with nigericin (10 μM) for different timepoints as indicated. (B-
1067 C) PBMCs were transfected with non-targeting control, or UCH-L1-specific siRNA, stimulated with
1068 LPS for 4 hours and nigericin for different timepoints as indicated. Production of IL-6 (B) and TNFα
1069 (C) in the supernatants from PBMCs were measured by ELISA.

1070
1071
1072
1073
1074
1075
1076
1077
1078
1079
1080
1081
1082
1083
1084
1085
1086
1087
1088

1089 **Figure S9**

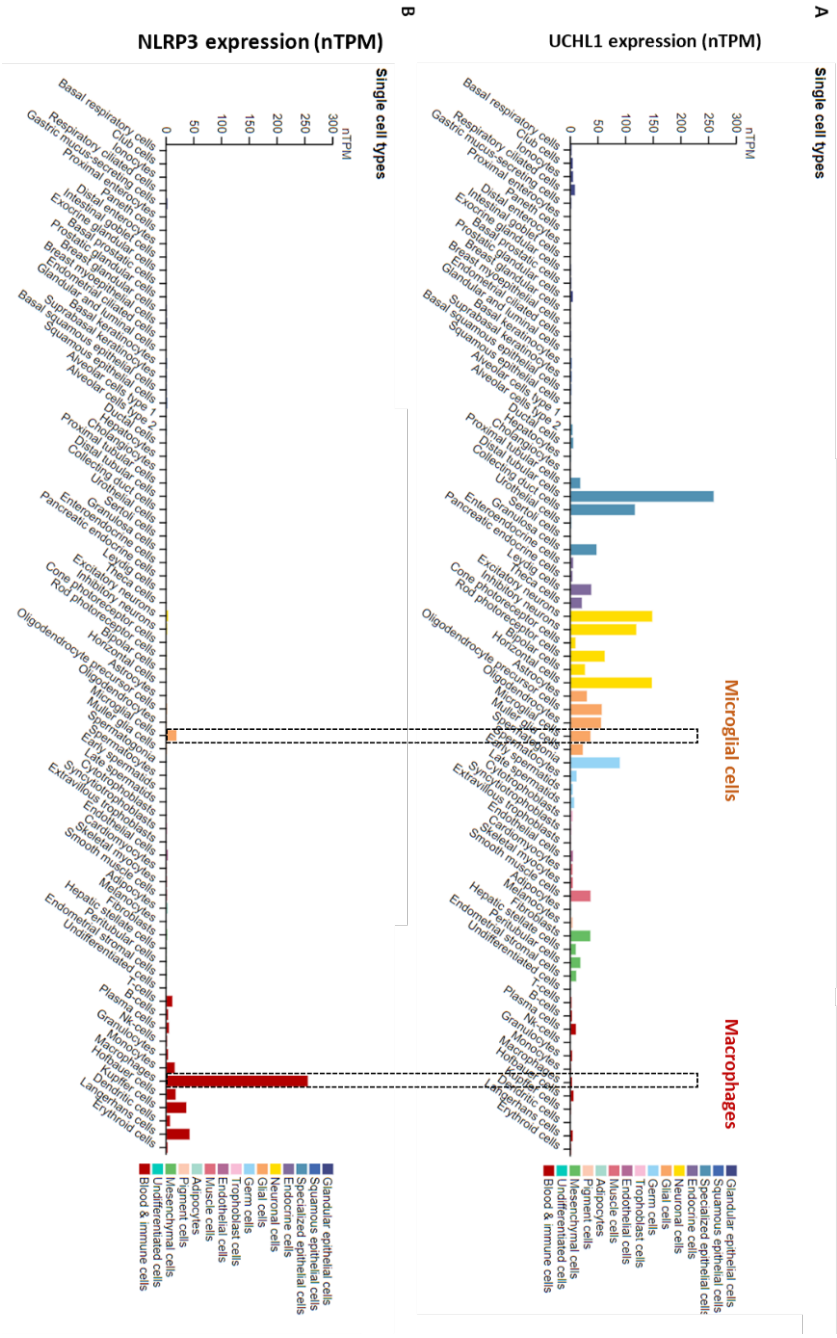


1090

1091

1092 **Figure S9 | RNA expression level of NLRP3 and UCH-L1 in different cell types**

1093 (A,B) A summary of normalized single cell RNA expression (nTPM) in different cell lines for UCH-

1094 L1 (A) and NLRP3 (B). Color-coding represents different cell type groups consisting of cell types with

1095 functional features in common (Data were retrieved from https://www.proteinatlas.org/ )

1096

1097

1098 **Figure S10**

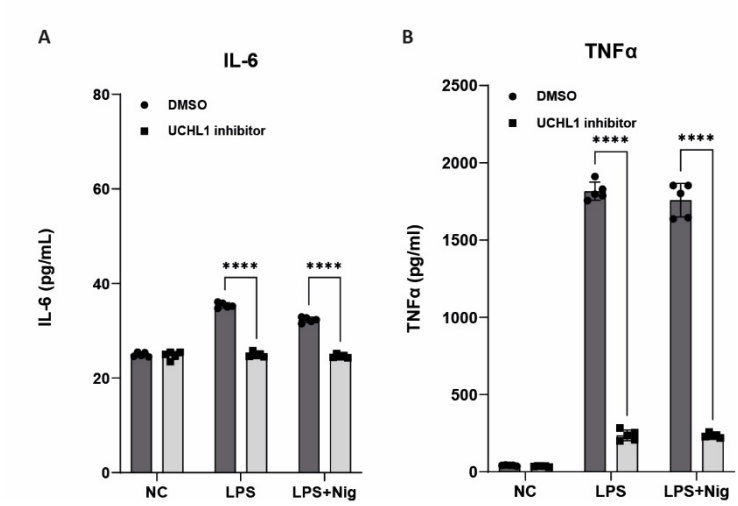


1099

1100 **Figure S10 | UCH-L1 inhibitor diminishes IL-6 and TNFα expression in THP-1 cells**

1101 (A, B) IL-6 (A) and TNFα (B) levels determined by ELISA from THP-1 cells treated with DMSO or
1102 0.3 μM IMP-1711-S. Cells were differentiated with PMA and primed with LPS 1 μg/mL) for 4 hours,
1103 followed by the treatment of nigericin (10 μM) for 45 minutes. The inhibitor or the DMSO were added
1104 at the same time with LPS. Error bars show the standard deviation of the mean. ****$p < 0.0001$
1105 (unpaired two-sided t-test).

1106

1107

1108

1109

1110

1111

1112

1113

1114

1115

1116

1117

1118

1119 **Figure S11**

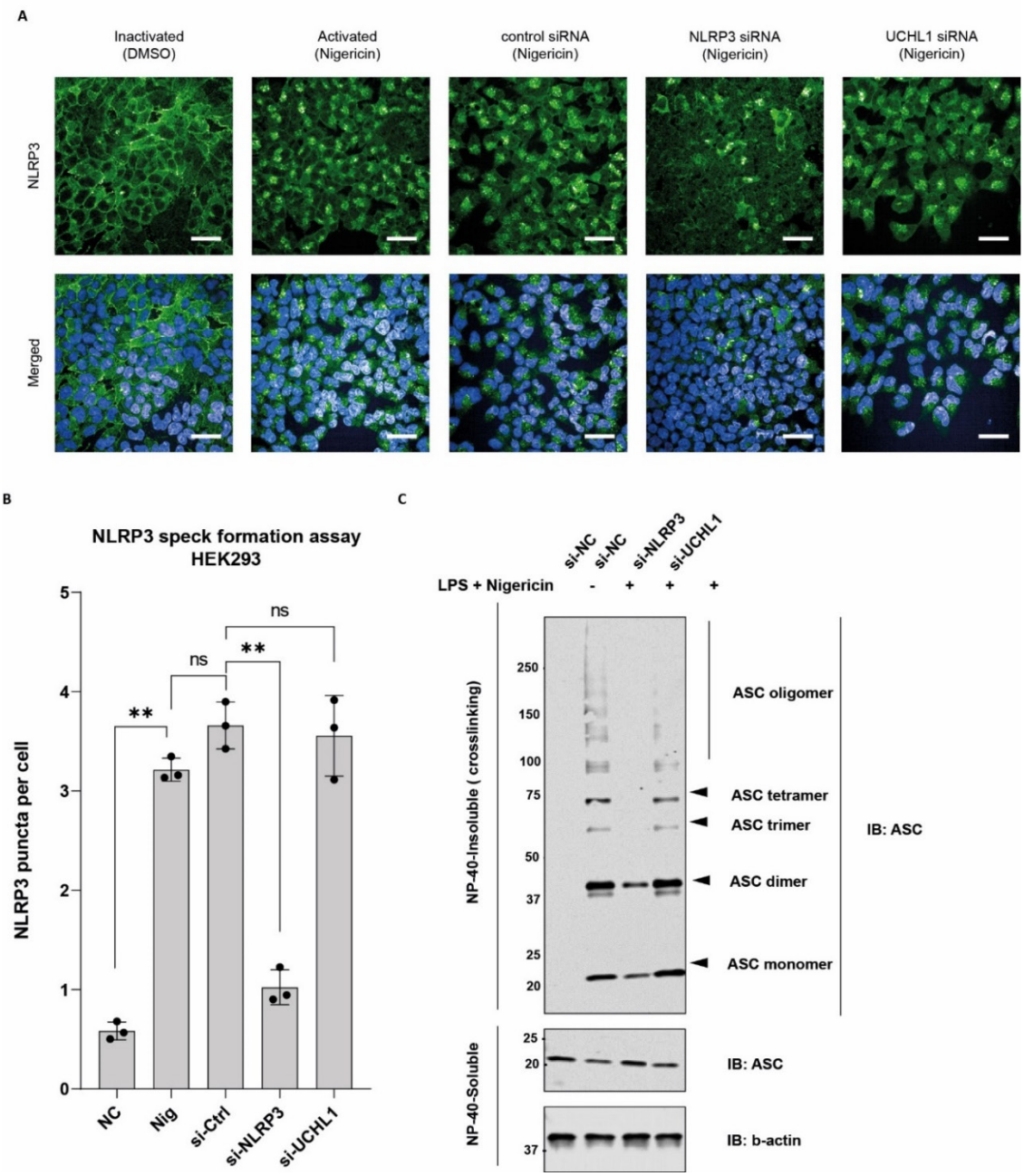


1120

1121 **Figure S11 | UCH-L1 is dispensable for NLRP3 puncta formation but partially alters ASC**
1122 **oligomerization**

1123 (A, B) flag-NLRP3 HEK293 stable cells were transfected with non-targeting control siRNA, NLRP3 or
1124 UCH-L1-specific siRNA. 48 hours after transfection, cells were treated with DMSO or 10 μM nigericin
1125 for 45 minutes. Subsequently, cells were stained with anti-flag antibody to measure the formation of
1126 NLRP3 puncta. (A) Representative fluorescence imaging of NLRP3 puncta using Opera Phenix Plus
1127 High-Content Screening System. Scale bars, 50 μm. (B) Quantitative analysis of the NLRP3 puncta
1128 formation (n = 3, mean ± s.d.). (C) Immunoblot analysis of ASC after DSS crosslinking in THP-1 cells
1129 transfected with non-targeting control siRNA, NLRP3 or UCH-L1-specific siRNA.

1130 **Figure S12**

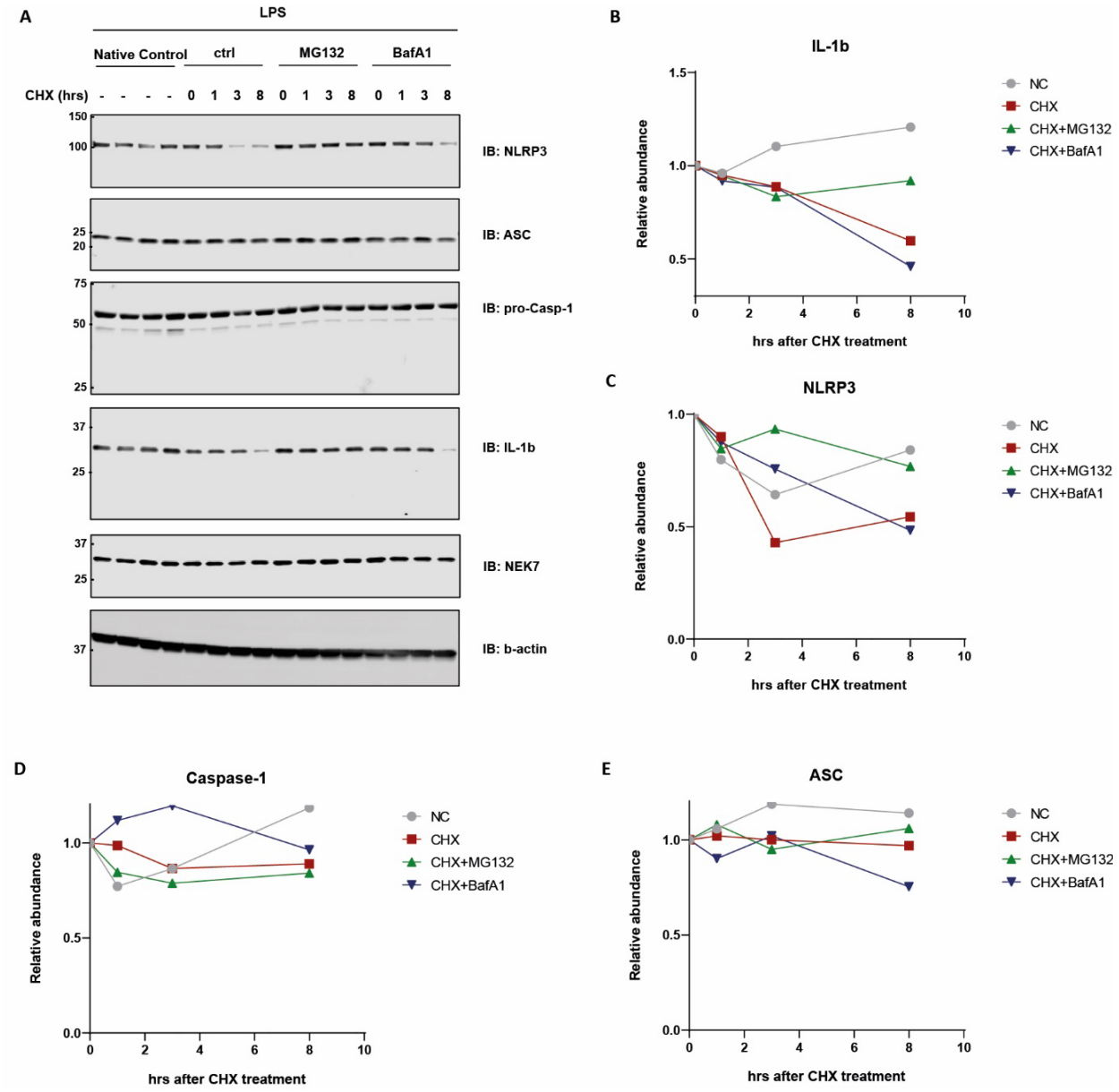


1131

1132

1133 **Figure S12 | Protein turnover of NLRP3 and IL-1β depend on the ubiquitin proteasome pathway**
1134 (A) PMA-differentiated THP-1 cells were primed with LPS (100ng/mL) for 4 hours and followed by
1135 the treatment of MG132 (20μM) or BafA1 (300nM) as indicated in the last 30 min alongside. Cells
1136 were then treated with cycloheximide (50μg/mL) for 1, 3 and 8 h as indicated. Cell lysates were
1137 collected and immunoblotted for the indicated antibodies. Immunoblotting from one representative
1138 experiment of three is shown. (B-E) Quantitative analysis of the western blotting results in (A).

1139

1140

1141 **Figure S13**

1142 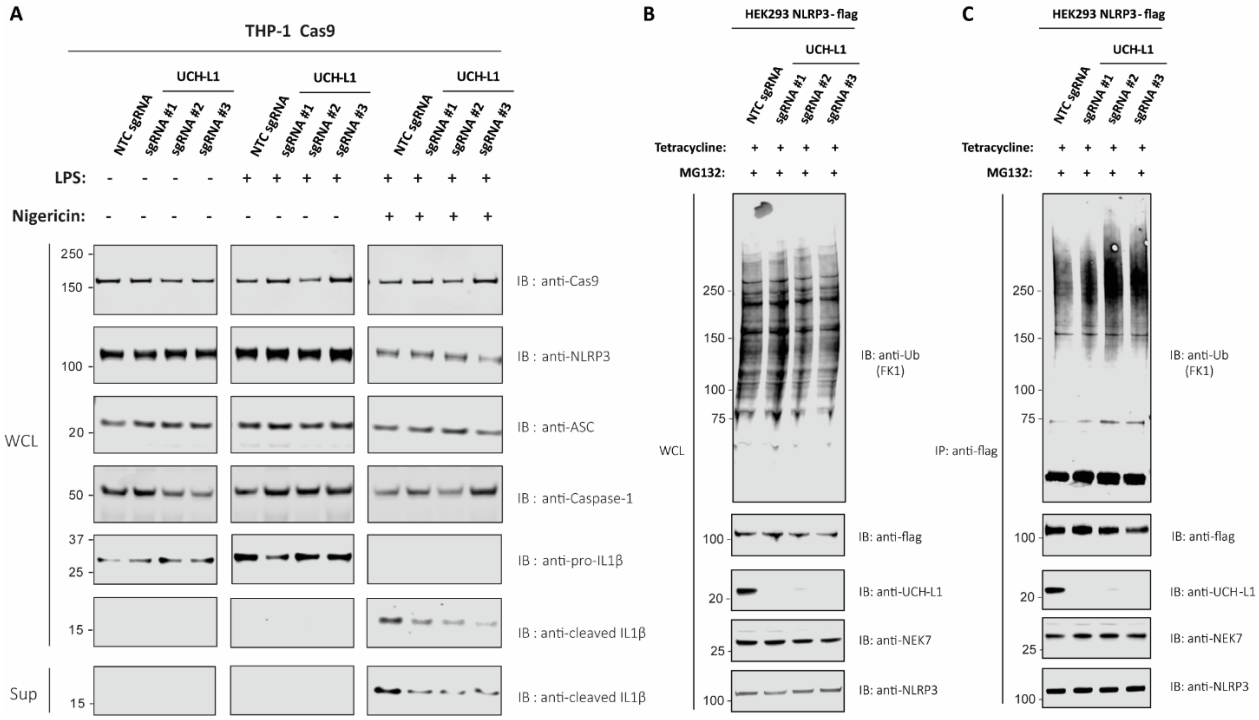


1143 **Figure S13 | UCH-L1 deficiency abrogates IL-1β production and alters NLRP3 ubiquitination**

1144 (A) THP-1 cells, transduced by lentiviruses encoding Cas9 and non-targeting control (NTC) sgRNA or
1145 sgRNA-1/2/3 targeting UCH-L1, were differentiated with PMA, primed with LPS for 4 hours and
1146 treated with nigericin for 45 minutes, as indicated. Whole cell lysates and supernatants were
1147 immunoblotted with indicated antibodies. (B-C) flag-NLRP3 HEK293 stable cell lines, transduced by
1148 lentiviruses encoding Cas9 and non-targeting control (NTC) sgRNA or sgRNA-1/2/3 targeting UCH-
1149 L1, were treated with MG132 (10 μM) for 6 hours. Whole cell lysates (A) and flag-NLRP3
1150 immunoprecipitated in RIPA lysis buffer (B) were analysed with indicated antibodies.

1151

1152

1153

1154

1155

1156

1157

1158

1159 **Table S1 | List of known NLRP3-interacting proteins curated from literature**

1160

| Interactor | Experimental System | Throughput | Organism | Reference |
|---|---|---|---|---|
| **HIST1H1B** | Affinity Capture-MS | High Throughput | Homo sapiens | PUBMED:26496610 |
| **HNRNPC** | Affinity Capture-MS | High Throughput | Homo sapiens | PUBMED:26496610 |
| **RBBP7** | Affinity Capture-MS | High Throughput | Homo sapiens | PUBMED:26496610 |
| **SNRPB** | Affinity Capture-MS | High Throughput | Homo sapiens | PUBMED:26496610 |
| **SPAST** | Affinity Capture-MS | High Throughput | Homo sapiens | PUBMED:26496610 |
| **TOP1** | Affinity Capture-MS | High Throughput | Homo sapiens | PUBMED:26496610 |
| **LTBP4** | Affinity Capture-MS | High Throughput | Homo sapiens | PUBMED:26496610 |
| **SMARCA5** | Affinity Capture-MS | High Throughput | Homo sapiens | PUBMED:26496610 |
| **GEMIN2** | Affinity Capture-MS | High Throughput | Homo sapiens | PUBMED:26496610 |
| **YBX3** | Affinity Capture-MS | High Throughput | Homo sapiens | PUBMED:26496610 |
| **AP3B1** | Affinity Capture-MS | High Throughput | Homo sapiens | PUBMED:26496610 |
| **PHF14** | Affinity Capture-MS | High Throughput | Homo sapiens | PUBMED:26496610 |
| **URB1** | Affinity Capture-MS | High Throughput | Homo sapiens | PUBMED:26496610 |
| **DNAJA2** | Affinity Capture-MS | High Throughput | Homo sapiens | PUBMED:26496610 |
| **CBX3** | Affinity Capture-MS | High Throughput | Homo sapiens | PUBMED:26496610 |
| **FBXO28** | Affinity Capture-MS | High Throughput | Homo sapiens | PUBMED:26496610 |
| **CBX5** | Affinity Capture-MS | High Throughput | Homo sapiens | PUBMED:26496610 |
| **MTCH1** | Affinity Capture-MS | High Throughput | Homo sapiens | PUBMED:26496610 |
| **PVRL3** | Affinity Capture-MS | High Throughput | Homo sapiens | PUBMED:26496610 |
| **FBXL6** | Affinity Capture-MS | High Throughput | Homo sapiens | PUBMED:26496610 |
| **UQCRQ** | Affinity Capture-MS | High Throughput | Homo sapiens | PUBMED:26496610 |
| **COPS7A** | Affinity Capture-MS | High Throughput | Homo sapiens | PUBMED:26496610 |
| **LUC7L3** | Affinity Capture-MS | High Throughput | Homo sapiens | PUBMED:26496610 |
| **GPATCH4** | Affinity Capture-MS | High Throughput | Homo sapiens | PUBMED:26496610 |
| **FEM1A** | Affinity Capture-MS | High Throughput | Homo sapiens | PUBMED:26496610 |
| **LUC7L** | Affinity Capture-MS | High Throughput | Homo sapiens | PUBMED:26496610 |

| Interactor | Experimental System | Throughput | Organism | Reference |
|---|---|---|---|---|
| **DMAP1** | Affinity Capture-MS | High Throughput | Homo sapiens | PUBMED:26496610 |
| **PHRF1** | Affinity Capture-MS | High Throughput | Homo sapiens | PUBMED:26496610 |
| **CCDC86** | Affinity Capture-MS | High Throughput | Homo sapiens | PUBMED:26496610 |
| **PCGF5** | Affinity Capture-MS | High Throughput | Homo sapiens | PUBMED:26496610 |
| **ZC3H8** | Affinity Capture-MS | High Throughput | Homo sapiens | PUBMED:26496610 |
| **KIAA2013** | Affinity Capture-MS | High Throughput | Homo sapiens | PUBMED:26496610 |
| **NLRP5** | Affinity Capture-MS | High Throughput | Homo sapiens | PUBMED:26496610 |
| **STUB1** | Affinity Capture-MS | Low Throughput | Homo sapiens | PUBMED:25594175 |
| **MARCH7** | Affinity Capture-MS | Low Throughput | Homo sapiens | PUBMED:25594175 |
| **UBR5** | Affinity Capture-MS | Low Throughput | Homo sapiens | PUBMED:25594175 |
| **CUL4A** | Affinity Capture-MS | High Throughput | Homo sapiens | PUBMED:30945288 |
| **CUL4B** | Affinity Capture-MS | High Throughput | Homo sapiens | PUBMED:30945288 |
| **VDR** | Affinity Capture-MS, Affinity Capture-Western, Reconstituted Complex | High Throughput | Homo sapiens | PUBMED:31866999 |
| **NLRC4** | Affinity Capture-Western | Low Throughput | Homo sapiens | PUBMED:15107016 |
| **SUGT1** | Affinity Capture-Western | Low Throughput | Homo sapiens | PUBMED:17435760 |
| **HSP90AA1** | Affinity Capture-Western | Low Throughput | Homo sapiens | PUBMED:17435760 |
| **DHX33** | Affinity Capture-Western | Low Throughput | Homo sapiens | PUBMED:25172487 |
| **ULK1** | Affinity Capture-Western | Low Throughput | Homo sapiens | PUBMED:26347139 |
| **MEFV** | Affinity Capture-Western | Low Throughput | Homo sapiens | PUBMED:26347139 |
| **HDAC6** | Affinity Capture-Western | Low Throughput | Homo sapiens | PUBMED:26471297 |
| **USP50** | Affinity Capture-Western | Low Throughput | Homo sapiens | PUBMED:28094437 |
| **ARIH2** | Affinity Capture-Western | Low Throughput | Homo sapiens | PUBMED:29021376 |
| **TXNIP** | Affinity Capture-Western, Two-hybrid | Low Throughput | Homo sapiens | PUBMED:28326454, PUBMED:30833078, PUBMED:32323100, PUBMED:32716108 |
| **RBX1** | Affinity Capture-Western | Low Throughput | Homo sapiens | PUBMED:30653357 |
| **FAM175B** | Affinity Capture-Western | Low Throughput | Homo sapiens | PUBMED:30787184 |
| **BRCC3** | Affinity Capture-Western | Low Throughput | Homo sapiens, Mus musculus | PUBMED:30787184, PUBMED:31866999, PUBMED:32941940 |

| Interactor | Experimental System | Throughput | Organism | Reference |
|---|---|---|---|---|
| **ORF8b** | Affinity Capture-Western | Low Throughput | Severe acute respiratory syndrome-related coronavirus | PUBMED:31231549 |
| **SRC** | Affinity Capture-Western | Low Throughput | Homo sapiens | PUBMED:31553908 |
| **NEK7** | Affinity Capture-Western | Low Throughput | Homo sapiens | PUBMED:31762063, PUBMED:31866999 |
| **Ppp2ca** | Affinity Capture-Western | Low Throughput | Homo sapiens | PUBMED:31866999 |
| **SQSTM1** | Affinity Capture-Western | Low Throughput | Homo sapiens | PUBMED:32003754 |
| **IL1B** | Affinity Capture-Western | Low Throughput | Homo sapiens | PUBMED:32597834 |
| **EIF3F** | Affinity Capture-Western | Low Throughput | Homo sapiens | PUBMED:33243234 |
| **USP13** | Affinity Capture-Western | Low Throughput | Homo sapiens | PUBMED:33243234 |
| **PSMB8** | Affinity Capture-Western | Low Throughput | Homo sapiens | PUBMED:32782149 |
| **PARK2** | Affinity Capture-Western | Low Throughput | Homo sapiens | PUBMED:33527027 |
| **BTRC** | Affinity Capture-Western | Low Throughput | Homo sapiens | PUBMED:33976226 |
| **TRIM24** | Affinity Capture-Western | Low Throughput | Homo sapiens | PUBMED:33724611 |
| **USP5** | Affinity Capture-Western | Low Throughput | Homo sapiens | PUBMED:34486483 |
| **TRIM28** | Affinity Capture-Western | Low Throughput | Homo sapiens | PUBMED:34373456 |
| **LYN** | Affinity Capture-Western | Low Throughput | Homo sapiens | PMID: 34699250 |
| **EIF2AK2** | Affinity Capture-Western | Low Throughput | Homo sapiens | PMID: 22801494 |
| **PRKD1/2/3** | Affinity Capture-Western | Low Throughput | Homo sapiens | PMID: 28716882 |
| **FBXL2** | Affinity Capture-Western, Biochemical Activity | Low Throughput | Homo sapiens | PUBMED:26037928 |
| **PYCARD** | Affinity Capture-Western, Co-localization | Low Throughput | Homo sapiens | PUBMED:30182366, PUBMED:32003754, PUBMED:32435622 |
| **P2RY2** | Affinity Capture-Western, Co-localization | Low Throughput | Homo sapiens | PUBMED:31553908 |
| **MAVS** | Affinity Capture-Western, Co-localization | Low Throughput | Homo sapiens | PMID: 23582325 |
| **NLRP11** | Affinity Capture-Western, Co-localization | Low Throughput | Homo sapiens | PMID: 35624206 |
| **CBLB** | Affinity Capture-Western, Reconstituted Complex | Low Throughput | Homo sapiens | PUBMED:31999304 |

| Interactor | Experimental System | Throughput | Organism | Reference |
|---|---|---|---|---|
| **RNF125** | Affinity Capture-Western, Reconstituted Complex | Low Throughput | Homo sapiens | PUBMED:31999304 |
| **STAMBP** | Biochemical Activity, Affinity Capture-Western | Low Throughput | Homo sapiens | PUBMED:32003754, PUBMED:33253913 |
| **MCFD2** | Co-fractionation | High Throughput | Homo sapiens | PUBMED:26344197 |
| **ARHGAP17** | Co-fractionation | High Throughput | Homo sapiens | PUBMED:26344197 |
| **SH3BP1** | Co-fractionation | High Throughput | Homo sapiens | PUBMED:26344197 |
| **CASP8** | Co-localization | Low Throughput | Homo sapiens | PUBMED:30182366 |
| **MARK4** | Co-localization | Low Throughput | Homo sapiens | PUBMED:31167564 |
| **HSPD1** | Proximity Label-MS | High Throughput | Homo sapiens | PUBMED:30021884 |
| **Rnf213** | Reconstituted Complex | High Throughput | Homo sapiens, Mus musculus | PUBMED:31999304 |
| **Trim21** | Reconstituted Complex | High Throughput | Homo sapiens, Mus musculus | PUBMED:31999304 |
| **Trim47** | Reconstituted Complex | High Throughput | Homo sapiens, Mus musculus | PUBMED:31999304 |
| **Trim14** | Reconstituted Complex | High Throughput | Homo sapiens, Mus musculus | PUBMED:31999304 |
| **ORF8** | Reconstituted Complex, Affinity Capture-Western | Low Throughput | Severe acute respiratory syndrome coronavirus 2 | DOI:10.1101/2021.12.02.470978 |
| **TRIM31** | Reconstituted Complex, Affinity Capture-Western, Biochemical Activity | Low Throughput | Homo sapiens | PUBMED:27929086 |
| **PGM1** | Two-hybrid | High Throughput | Homo sapiens | PUBMED:30653357 |
| **ATP1B3** | Two-hybrid | High Throughput | Homo sapiens | PUBMED:30653357 |
| **CUL1** | Two-hybrid, Affinity Capture-Western, Co-localization, PCA | High Throughput | Homo sapiens | PUBMED:30653357 |
| **PXN** | Two-hybrid, Affinity Capture-Western, Reconstituted Complex, Co-localization | Low Throughput | Homo sapiens | PUBMED:33243234 |
| **FAF1** | Two-hybrid, Reconstituted Complex, Affinity Capture-Western | Low Throughput | Homo sapiens | PUBMED:17046979 |

1165 **Table S2 | List of the Golgi membrane proteins differentially captured by NLRP3-APEX2 during**
1166 **nigericin-induced inflammasome assembly**

| Protein IDs | Protein names | Gene names | Peptides | Unique peptides | Sequence coverage [%] |
|---|---|---|---|---|---|
| O14828 | Secretory carrier-associated membrane protein 3 | SCAMP3 | 11 | 11 | 42.1 |
| O94979 | Protein transport protein Sec31A | SEC31A | 26 | 26 | 23 |
| O95487 | Protein transport protein Sec24B | SEC24B | 23 | 23 | 22.7 |
| P22059 | Oxysterol-binding protein 1 | OSBP | 20 | 20 | 33 |
| P53992 | Protein transport protein Sec24C | SEC24C | 25 | 24 | 31.9 |
| P61019;Q8WUD1 | Ras-related protein Rab-2A;Ras-related protein Rab-2B | RAB2A;RAB2B | 6 | 6 | 37.7 |
| P61106 | Ras-related protein Rab-14 | RAB14 | 12 | 12 | 65.6 |
| Q00610 | Clathrin heavy chain 1 | CLTC | 57 | 57 | 39.6 |
| Q08379 | Golgin subfamily A member 2 | GOLGA2 | 22 | 22 | 28 |
| Q10567 | AP-1 complex subunit beta-1 | AP1B1 | 19 | 5 | 21.6 |
| Q12907 | Vesicular integral-membrane protein VIP36 | LMAN2 | 11 | 11 | 37.9 |
| Q14789 | Golgin subfamily B member 1 | GOLGB1 | 106 | 106 | 45.4 |
| Q15436 | Protein transport protein Sec23A | SEC23A | 20 | 17 | 35.7 |
| Q15437 | Protein transport protein Sec23B | SEC23B | 24 | 21 | 37.2 |
| Q86Y82 | Syntaxin-12 | STX12 | 8 | 8 | 37.7 |
| Q8NF37 | Lysophosphatidylcholine acyltransferase 1 | LPCAT1 | 4 | 4 | 10.7 |
| Q8TBA6 | Golgin subfamily A member 5 | GOLGA5 | 22 | 22 | 41.9 |
| Q9BXF6 | Rab11 family-interacting protein 5 | RAB11FIP5 | 12 | 12 | 32.3 |
| Q9H0U4;Q92928 | Ras-related protein Rab-1B;Putative Ras-related protein Rab-1C | RAB1B;RAB1C | 4 | 2 | 29.4 |
| Q9NRW7 | Vacuolar protein sorting-associated protein 45 | VPS45 | 11 | 11 | 19.6 |
| Q9NTJ5 | Phosphatidylinositide phosphatase SAC1 | SACM1L | 11 | 11 | 19.3 |
| Q9Y2H6 | Fibronectin type-III domain-containing protein 3A | FNDC3A | 7 | 7 | 8.3 |

1167

1168

1169

1170

1171 **Table S3 | Human DUB siRNA screening in THP-1 cells**

**LPS**

| Rank | Gene | Normalized IL1b | z-score |
|---|---|---|---|
| 1 | TNFAIP3 | 2.334 | 3.451 |
| 2 | UCHL3 | 2.217 | 2.720 |
| 3 | CYLD | 2.103 | 2.013 |
| 4 | USP8 | 2.016 | 1.470 |
| 5 | JOSD2 | 2.010 | 1.432 |
| 6 | USP38 | 1.996 | 1.343 |
| 7 | USP18 | 1.992 | 1.320 |
| 8 | JOSD1 | 1.992 | 1.319 |
| 9 | USP40 | 1.983 | 1.261 |
| 10 | OTUD6B | 1.977 | 1.228 |
| 11 | ZRANB1 | 1.976 | 1.221 |
| 12 | OTUD7A | 1.967 | 1.162 |
| 13 | OTUD7B | 1.956 | 1.098 |
| 14 | USP33 | 1.951 | 1.066 |
| 15 | USP46 | 1.938 | 0.984 |
| 16 | USP43 | 1.923 | 0.892 |
| 17 | STAMBPL1 | 1.914 | 0.838 |
| 18 | OTUB2 | 1.902 | 0.759 |
| 19 | USPL1 | 1.900 | 0.746 |
| 20 | OTUD5 | 1.898 | 0.736 |
| 21 | USP21 | 1.895 | 0.715 |
| 22 | USP48 | 1.893 | 0.704 |
| 23 | USP3 | 1.870 | 0.563 |
| 24 | STAMBP | 1.867 | 0.542 |
| 25 | USP45 | 1.863 | 0.518 |
| 26 | USP27X | 1.863 | 0.518 |
| 27 | USP11 | 1.860 | 0.501 |
| 28 | USP13 | 1.856 | 0.472 |
| 29 | COPS5 | 1.854 | 0.464 |
| 30 | USP6 | 1.848 | 0.422 |
| 31 | MYSM1 | 1.845 | 0.403 |
| 32 | USP50 | 1.838 | 0.361 |
| 33 | PAN2 | 1.832 | 0.326 |
| 34 | SENP2 | 1.832 | 0.323 |
| 35 | USP5 | 1.831 | 0.317 |
| 36 | USP24 | 1.831 | 0.315 |
| 37 | PRPF8 | 1.821 | 0.259 |
| 38 | UFD1L | 1.816 | 0.226 |
| 39 | USP1 | 1.814 | 0.214 |
| 40 | VCPIP1 | 1.813 | 0.208 |
| 41 | PSMD14 | 1.811 | 0.197 |
| 42 | UBL4A | 1.801 | 0.131 |
| 43 | UCHL5 | 1.800 | 0.123 |

**LPS + Nigericin**

| Rank | Gene | Normalized IL1b | z-score |
|---|---|---|---|
| 1 | STAMBP | 3.064 | 2.238 |
| 2 | USP39 | 2.966 | 2.015 |
| 3 | ZRANB1 | 2.924 | 1.917 |
| 4 | USP17L2 | 2.899 | 1.861 |
| 5 | USP38 | 2.875 | 1.806 |
| 6 | USP47 | 2.846 | 1.740 |
| 7 | USP25 | 2.846 | 1.739 |
| 8 | UBTD1 | 2.794 | 1.620 |
| 9 | UCK2 | 2.775 | 1.576 |
| 10 | UCHL3 | 2.727 | 1.465 |
| 11 | COPS5 | 2.698 | 1.399 |
| 12 | USP14 | 2.689 | 1.379 |
| 13 | USP8 | 2.687 | 1.375 |
| 14 | USP33 | 2.665 | 1.323 |
| 15 | ATXN3 | 2.656 | 1.304 |
| 16 | USP31 | 2.608 | 1.194 |
| 17 | UBTD2 | 2.606 | 1.187 |
| 18 | USP37 | 2.518 | 0.986 |
| 19 | USP43 | 2.515 | 0.981 |
| 20 | OTUD1 | 2.514 | 0.976 |
| 21 | USP34 | 2.505 | 0.957 |
| 22 | USP5 | 2.476 | 0.890 |
| 23 | FBXO8 | 2.452 | 0.834 |
| 24 | USP3 | 2.449 | 0.828 |
| 25 | USP22 | 2.433 | 0.792 |
| 26 | STAMBPL1 | 2.397 | 0.709 |
| 27 | BRCC3 | 2.389 | 0.691 |
| 28 | USP42 | 2.366 | 0.637 |
| 29 | USP32 | 2.357 | 0.617 |
| 30 | USP24 | 2.340 | 0.579 |
| 31 | USPL1 | 2.320 | 0.532 |
| 32 | YOD1 | 2.315 | 0.521 |
| 33 | USP54 | 2.313 | 0.516 |
| 34 | JOSD2 | 2.293 | 0.471 |
| 35 | UCHL5 | 2.272 | 0.422 |
| 36 | USP30 | 2.254 | 0.381 |
| 37 | USP40 | 2.237 | 0.342 |
| 38 | USP27X | 2.233 | 0.332 |
| 39 | USP26 | 2.206 | 0.271 |
| 40 | PRPF8 | 2.200 | 0.258 |
| 41 | UFD1L | 2.189 | 0.233 |
| 42 | USP35 | 2.184 | 0.220 |
| 43 | OTUD4 | 2.153 | 0.150 |

**LPS**

| Rank | Gene | Normalized IL1b | z-score |
|---|---|---|---|
| 44 | UBTD2 | 1.796 | 0.102 |
| 45 | USP39 | 1.791 | 0.067 |
| 46 | USP29 | 1.789 | 0.059 |
| 47 | BRCC3 | 1.785 | 0.032 |
| 48 | USP28 | 1.767 | -0.077 |
| 49 | USP32 | 1.763 | -0.107 |
| 50 | USP19 | 1.754 | -0.164 |
| 51 | USP7 | 1.752 | -0.173 |
| 52 | USP41 | 1.748 | -0.200 |
| 53 | MPND | 1.745 | -0.214 |
| 54 | USP34 | 1.744 | -0.220 |
| 55 | UBTD1 | 1.738 | -0.260 |
| 56 | USP4 | 1.738 | -0.262 |
| 57 | USP10 | 1.736 | -0.273 |
| 58 | USP25 | 1.730 | -0.307 |
| 59 | USP44 | 1.729 | -0.317 |
| 60 | USP9Y | 1.729 | -0.317 |
| 61 | FBXO8 | 1.722 | -0.362 |
| 62 | USP12 | 1.721 | -0.368 |
| 63 | YOD1 | 1.721 | -0.369 |
| 64 | USP15 | 1.718 | -0.388 |
| 65 | UBL5 | 1.716 | -0.397 |
| 66 | USP22 | 1.715 | -0.405 |
| 67 | PARP11 | 1.714 | -0.408 |
| 68 | USP30 | 1.713 | -0.416 |
| 69 | USP49 | 1.710 | -0.436 |
| 70 | UEVLD | 1.710 | -0.437 |
| 71 | OTUB1 | 1.699 | -0.501 |
| 72 | USP17L2 | 1.692 | -0.545 |
| 73 | ATXN3 | 1.690 | -0.557 |
| 74 | UBL3 | 1.689 | -0.563 |
| 75 | USP47 | 1.683 | -0.603 |
| 76 | USP14 | 1.680 | -0.619 |
| 77 | USP42 | 1.680 | -0.622 |
| 78 | USP54 | 1.678 | -0.634 |
| 79 | FBXO7 | 1.672 | -0.671 |
| 80 | USP35 | 1.660 | -0.743 |
| 81 | USP16 | 1.657 | -0.765 |
| 82 | USP53 | 1.654 | -0.781 |
| 83 | USP2 | 1.654 | -0.782 |
| 84 | USP31 | 1.626 | -0.956 |
| 85 | BAP1 | 1.626 | -0.959 |
| 86 | USP51 | 1.617 | -1.017 |
| 87 | USP37 | 1.616 | -1.022 |
| 88 | OTUD1 | 1.578 | -1.258 |

**LPS + Nigericin**

| Rank | Gene | Normalized IL1b | z-score |
|---|---|---|---|
| 44 | USP15 | 2.146 | 0.133 |
| 45 | USP36 | 2.126 | 0.087 |
| 46 | PARP11 | 2.098 | 0.023 |
| 47 | USP18 | 2.082 | -0.014 |
| 48 | USP2 | 2.063 | -0.058 |
| 49 | PAN2 | 1.986 | -0.234 |
| 50 | UBL5 | 1.869 | -0.501 |
| 51 | USP1 | 1.862 | -0.518 |
| 52 | BAP1 | 1.826 | -0.601 |
| 53 | USP48 | 1.822 | -0.609 |
| 54 | SENP2 | 1.814 | -0.627 |
| 55 | USP9Y | 1.796 | -0.670 |
| 56 | OTUD6B | 1.796 | -0.670 |
| 57 | FBXO7 | 1.792 | -0.679 |
| 58 | USP16 | 1.785 | -0.694 |
| 59 | USP21 | 1.777 | -0.712 |
| 60 | USP29 | 1.769 | -0.733 |
| 61 | USP50 | 1.753 | -0.768 |
| 62 | UBL4A | 1.747 | -0.781 |
| 63 | USP46 | 1.741 | -0.795 |
| 64 | CYLD | 1.739 | -0.800 |
| 65 | USP28 | 1.739 | -0.801 |
| 66 | USP45 | 1.736 | -0.808 |
| 67 | OTUB2 | 1.730 | -0.820 |
| 68 | MYSM1 | 1.726 | -0.829 |
| 69 | USP49 | 1.715 | -0.855 |
| 70 | USP12 | 1.714 | -0.858 |
| 71 | UBL3 | 1.683 | -0.930 |
| 72 | USP44 | 1.679 | -0.938 |
| 73 | OTUD7A | 1.675 | -0.948 |
| 74 | TNFAIP3 | 1.668 | -0.963 |
| 75 | PSMD14 | 1.667 | -0.965 |
| 76 | USP20 | 1.664 | -0.972 |
| 77 | USP41 | 1.664 | -0.972 |
| 78 | USP4 | 1.664 | -0.973 |
| 79 | USP19 | 1.660 | -0.981 |
| 80 | MPND | 1.660 | -0.981 |
| 81 | OTUD5 | 1.658 | -0.987 |
| 82 | USP9X | 1.657 | -0.989 |
| 83 | USP53 | 1.654 | -0.996 |
| 84 | USP13 | 1.648 | -1.010 |
| 85 | JOSD1 | 1.647 | -1.011 |
| 86 | VCPIP1 | 1.640 | -1.028 |
| 87 | USP7 | 1.622 | -1.068 |
| 88 | UCHL1 | 1.617 | -1.079 |

**LPS**

| Rank | Gene | Normalized IL1b | z-score |
|---|---|---|---|
| 89 | OTUD4 | 1.577 | -1.262 |
| 90 | UBR1 | 1.520 | -1.617 |
| 91 | UCK2 | 1.513 | -1.663 |
| 92 | USP9X | 1.483 | -1.845 |
| 93 | USP20 | 1.453 | -2.034 |
| 94 | USP36 | 1.447 | -2.074 |
| 95 | UCHL1 | 1.413 | -2.286 |
| 96 | USP26 | 1.316 | -2.887 |

**LPS + Nigericin**

| Rank | Gene | Normalized IL1b | z-score |
|---|---|---|---|
| 89 | UEVLD | 1.617 | -1.081 |
| 90 | OTUB1 | 1.613 | -1.088 |
| 91 | USP11 | 1.605 | -1.108 |
| 92 | USP51 | 1.600 | -1.118 |
| 93 | OTUD7B | 1.587 | -1.149 |
| 94 | UBR1 | 1.548 | -1.238 |
| 95 | USP6 | 1.547 | -1.240 |
| 96 | USP10 | 1.539 | -1.259 |

1192 **References**


1193 Akther, M., Haque, M.E., Park, J., Kang, T.B., and Lee, K.H. (2021). NLRP3 Ubiquitination-A New
1194 Approach to Target NLRP3 Inflammasome Activation. Int J Mol Sci *22*.
1195 Bednash, J.S., Johns, F., Patel, N., Smail, T.R., Londino, J.D., and Mallampalli, R.K. (2021). The
1196 deubiquitinase STAMBP modulates cytokine secretion through the NLRP3 inflammasome. Cell Signal
1197 *79*, 109859.
1198 Bordon, Y. (2019). Trans-Golgi network breaks away to activate NLRP3. Nat Rev Immunol *19*, 68-69.
1199 Bruntraeger, M., Byrne, M., Long, K., and Bassett, A.R. (2019). Editing the Genome of Human Induced
1200 Pluripotent Stem Cells Using CRISPR/Cas9 Ribonucleoprotein Complexes. Methods Mol Biol *1961*, 153-
1201 183.
1202 Cao, D.Y., Zhang, Z.H., Li, R.Z., Shi, X.K., Xi, R.Y., Zhang, G.L., Li, F., and Wang, F. (2022). A small molecule
1203 inhibitor of caspase-1 inhibits NLRP3 inflammasome activation and pyroptosis to alleviate gouty
1204 inflammation. Immunol Lett *244*, 28-39.
1205 Chen, J., and Chen, Z.J. (2018). PtdIns4P on dispersed trans-Golgi network mediates NLRP3
1206 inflammasome activation. Nature *564*, 71-76.
1207 Davis, S., Charles, P.D., He, L., Mowlds, P., Kessler, B.M., and Fischer, R. (2017). Expanding Proteome
1208 Coverage with CHarge Ordered Parallel Ion aNalysis (CHOPIN) Combined with Broad Specificity
1209 Proteolysis. J Proteome Res *16*, 1288-1299.
1210 Deutsch, E.W., Bandeira, N., Perez-Riverol, Y., Sharma, V., Carver, J.J., Mendoza, L., Kundu, D.J., Wang,
1211 S., Bandla, C., Kamatchinathan, S*., et al.* (2023). The ProteomeXchange consortium at 10 years: 2023
1212 update. Nucleic Acids Res *51*, D1539-D1548.
1213 Duong, B.H., Onizawa, M., Oses-Prieto, J.A., Advincula, R., Burlingame, A., Malynn, B.A., and Ma, A.
1214 (2015). A20 restricts ubiquitination of pro-interleukin-1beta protein complexes and suppresses NLRP3
1215 inflammasome activity. Immunity *42*, 55-67.
1216 Fox, D., and Man, S.M. (2019). DDX3X: stressing the NLRP3 inflammasome. Cell Res *29*, 969-970.
1217 Gross, O., Yazdi, A.S., Thomas, C.J., Masin, M., Heinz, L.X., Guarda, G., Quadroni, M., Drexler, S.K., and
1218 Tschopp, J. (2012). Inflammasome activators induce interleukin-1alpha secretion via distinct pathways
1219 with differential requirement for the protease function of caspase-1. Immunity *36*, 388-400.
1220 Guo, Y., Li, L., Xu, T., Guo, X., Wang, C., Li, Y., Yang, Y., Yang, D., Sun, B., Zhao, X*., et al.* (2020). HUWE1
1221 mediates inflammasome activation and promotes host defense against bacterial infection. J Clin Invest
1222 *130*, 6301-6316.
1223 Hai, B., Mao, T., Du, C., Jia, F., Liu, Y., Song, Q., Pan, X., Liu, X., and Zhu, B. (2022). USP14 promotes
1224 pyroptosis of human annulus fibrosus cells derived from patients with intervertebral disc
1225 degeneration through deubiquitination of NLRP3. Acta Biochim Biophys Sin (Shanghai) *54*, 1-11.
1226 Ham, S.J., Lee, D., Xu, W.J., Cho, E., Choi, S., Min, S., Park, S., and Chung, J. (2021). Loss of UCHL1
1227 rescues the defects related to Parkinson's disease by suppressing glycolysis. Sci Adv *7*.
1228 Hamilton, C., and Anand, P.K. (2019). Right place, right time: localisation and assembly of the NLRP3
1229 inflammasome. F1000Res *8*.
1230 He, Y., Zeng, M.Y., Yang, D., Motro, B., and Nunez, G. (2016). NEK7 is an essential mediator of NLRP3
1231 activation downstream of potassium efflux. Nature *530*, 354-357.
1232 Huang, Y., He, S., Chen, Y., Sheng, J., Fu, Y., Du, X., Yang, Y., Liu, H., Han, Z., Huang, Y*., et al.* (2022).
1233 UCHL1 Promoted Polarization of M1 Macrophages by Regulating the PI3K/AKT Signaling Pathway. J
1234 Inflamm Res *15*, 735-746.
1235 Kummari, E., Alugubelly, N., Hsu, C.Y., Dong, B., Nanduri, B., and Edelmann, M.J. (2015). Activity-Based
1236 Proteomic Profiling of Deubiquitinating Enzymes in Salmonella-Infected Macrophages Leads to
1237 Identification of Putative Function of UCH-L5 in Inflammasome Regulation. PLoS One *10*, e0135531.
1238 Lambert, J.P., Tucholska, M., Go, C., Knight, J.D., and Gingras, A.C. (2015). Proximity biotinylation and
1239 affinity purification are complementary approaches for the interactome mapping of chromatin-
1240 associated protein complexes. J Proteomics *118*, 81-94.

Lawlor, K.E., Khan, N., Mildenhall, A., Gerlic, M., Croker, B.A., D'Cruz, A.A., Hall, C., Kaur Spall, S., Anderton, H., Masters, S.L.*, et al.* (2015). RIPK3 promotes cell death and NLRP3 inflammasome activation in the absence of MLKL. Nat Commun *6*, 6282.

Liang, Z., Damianou, A., Di Daniel, E., and Kessler, B.M. (2021). Inflammasome activation controlled by the interplay between post-translational modifications: emerging drug target opportunities. Cell Commun Signal *19*, 23.

Liu, Y., Fallon, L., Lashuel, H.A., Liu, Z., and Lansbury, P.T., Jr. (2002). The UCH-L1 gene encodes two opposing enzymatic activities that affect alpha-synuclein degradation and Parkinson's disease susceptibility. Cell *111*, 209-218.

Lopez-Castejon, G. (2020). Control of the inflammasome by the ubiquitin system. FEBS J *287*, 11-26.

Lopez-Castejon, G., and Edelmann, M.J. (2016). Deubiquitinases: Novel Therapeutic Targets in Immune Surveillance? Mediators Inflamm *2016*, 3481371.

Lopez-Castejon, G., Luheshi, N.M., Compan, V., High, S., Whitehead, R.C., Flitsch, S., Kirov, A., Prudovsky, I., Swanton, E., and Brough, D. (2013). Deubiquitinases regulate the activity of caspase-1 and interleukin-1beta secretion via assembly of the inflammasome. J Biol Chem *288*, 2721-2733.

Mark Kemp, M.S., Alison Jones (2017). Cyanopyrrolidines as Dub Inhibitors for the Treatment of Cancer.

Martinon, F., Burns, K., and Tschopp, J. (2002). The inflammasome: a molecular platform triggering activation of inflammatory caspases and processing of proIL-beta. Mol Cell *10*, 417-426.

Mellacheruvu, D., Wright, Z., Couzens, A.L., Lambert, J.P., St-Denis, N.A., Li, T., Miteva, Y.V., Hauri, S., Sardiu, M.E., Low, T.Y.*, et al.* (2013). The CRAPome: a contaminant repository for affinity purification-mass spectrometry data. Nat Methods *10*, 730-736.

Mondal, M., Conole, D., Nautiyal, J., and Tate, E.W. (2022a). UCHL1 as a novel target in breast cancer: emerging insights from cell and chemical biology. Brit J Cancer *126*, 24-33.

Mondal, M., Conole, D., Nautiyal, J., and Tate, E.W. (2022b). UCHL1 as a novel target in breast cancer: emerging insights from cell and chemical biology. Br J Cancer *126*, 24-33.

Olie, C.S., Pinto-Fernandez, A., Damianou, A., Vendrell, I., Mei, H., den Hamer, B., van der Wal, E., de Greef, J.C., Raz, V., and Kessler, B.M. (2023). USP18 is an essential regulator of muscle cell differentiation and maturation. Cell Death Dis *14*, 231.

Oughtred, R., Rust, J., Chang, C., Breitkreutz, B.J., Stark, C., Willems, A., Boucher, L., Leung, G., Kolas, N., Zhang, F.*, et al.* (2021). The BioGRID database: A comprehensive biomedical resource of curated protein, genetic, and chemical interactions. Protein Sci *30*, 187-200.

Oughtred, R., Stark, C., Breitkreutz, B.J., Rust, J., Boucher, L., Chang, C., Kolas, N., O'Donnell, L., Leung, G., McAdam, R.*, et al.* (2019). The BioGRID interaction database: 2019 update. Nucleic Acids Res *47*, D529-D541.

Palazon-Riquelme, P., Worboys, J.D., Green, J., Valera, A., Martin-Sanchez, F., Pellegrini, C., Brough, D., and Lopez-Castejon, G. (2018). USP7 and USP47 deubiquitinases regulate NLRP3 inflammasome activation. EMBO Rep *19*.

Paludan, S.R., Pradeu, T., Masters, S.L., and Mogensen, T.H. (2021). Constitutive immune mechanisms: mediators of host defence and immune regulation. Nat Rev Immunol *21*, 137-150.

Panicker, N., Sarkar, S., Harischandra, D.S., Neal, M., Kam, T.I., Jin, H., Saminathan, H., Langley, M., Charli, A., Samidurai, M.*, et al.* (2019). Fyn kinase regulates misfolded alpha-synuclein uptake and NLRP3 inflammasome activation in microglia. J Exp Med *216*, 1411-1430.

Panyain, N., Godinat, A., Lanyon-Hogg, T., Lachiondo-Ortega, S., Will, E.J., Soudy, C., Mondal, M., Mason, K., Elkhalifa, S., Smith, L.M.*, et al.* (2020). Discovery of a Potent and Selective Covalent Inhibitor and Activity-Based Probe for the Deubiquitylating Enzyme UCHL1, with Antifibrotic Activity. J Am Chem Soc *142*, 12020-12026.

Panyain, N., Godinat, A., Thawani, A.R., Lachiondo-Ortega, S., Mason, K., Elkhalifa, S., Smith, L.M., Harrigan, J.A., and Tate, E.W. (2021). Activity-based protein profiling reveals deubiquitinase and aldehyde dehydrogenase targets of a cyanopyrrolidine probe. RSC Med Chem *12*, 1935-1943.

Perez-Riverol, Y., Bai, J., Bandla, C., Garcia-Seisdedos, D., Hewapathirana, S., Kamatchinathan, S., Kundu, D.J., Prakash, A., Frericks-Zipper, A., Eisenacher, M.*, et al.* (2022). The PRIDE database resources in 2022: a hub for mass spectrometry-based proteomics evidences. Nucleic Acids Res *50*, D543-D552.

Py, B.F., Kim, M.S., Vakifahmetoglu-Norberg, H., and Yuan, J. (2013). Deubiquitination of NLRP3 by BRCC3 critically regulates inflammasome activity. Mol Cell *49*, 331-338.

Qin, W., Cho, K.F., Cavanagh, P.E., and Ting, A.Y. (2021). Deciphering molecular interactions by proximity labeling. Nat Methods *18*, 133-143.

Qu, Z., Zhou, J., Zhou, Y., Xie, Y., Jiang, Y., Wu, J., Luo, Z., Liu, G., Yin, L., and Zhang, X.L. (2020). Mycobacterial EST12 activates a RACK1-NLRP3-gasdermin D pyroptosis-IL-1beta immune pathway. Sci Adv *6*.

Ramachandran, A., Kumar, B., Waris, G., and Everly, D. (2021). Deubiquitination and Activation of the NLRP3 Inflammasome by UCHL5 in HCV-Infected Cells. Microbiol Spectr *9*, e0075521.

Ren, G., Zhang, X., Xiao, Y., Zhang, W., Wang, Y., Ma, W., Wang, X., Song, P., Lai, L., Chen, H.*, et al.* (2019). ABRO1 promotes NLRP3 inflammasome activation through regulation of NLRP3 deubiquitination. EMBO J *38*.

Samir, P., Kesavardhana, S., Patmore, D.M., Gingras, S., Malireddi, R.K.S., Karki, R., Guy, C.S., Briard, B., Place, D.E., Bhattacharya, A.*, et al.* (2019). DDX3X acts as a live-or-die checkpoint in stressed cells by regulating NLRP3 inflammasome. Nature *573*, 590-594.

Shao, B.Z., Xu, Z.Q., Han, B.Z., Su, D.F., and Liu, C. (2015). NLRP3 inflammasome and its inhibitors: a review. Front Pharmacol *6*, 262.

Song, A., Hazlett, Z., Abeykoon, D., Dortch, J., Dillon, A., Curtiss, J., Martinez, S.B., Hill, C.P., Yu, C., Huang, L.*, et al.* (2021). Branched ubiquitin chain binding and deubiquitination by UCH37 facilitate proteasome clearance of stress-induced inclusions. Elife *10*.

Song, H., Liu, B., Huai, W., Yu, Z., Wang, W., Zhao, J., Han, L., Jiang, G., Zhang, L., Gao, C., and Zhao, W. (2016). The E3 ubiquitin ligase TRIM31 attenuates NLRP3 inflammasome activation by promoting proteasomal degradation of NLRP3. Nat Commun *7*, 13727.

Song, H., Zhao, C., Yu, Z., Li, Q., Yan, R., Qin, Y., Jia, M., and Zhao, W. (2020). UAF1 deubiquitinase complexes facilitate NLRP3 inflammasome activation by promoting NLRP3 expression. Nat Commun *11*, 6042.

Stark, C., Breitkreutz, B.J., Reguly, T., Boucher, L., Breitkreutz, A., and Tyers, M. (2006). BioGRID: a general repository for interaction datasets. Nucleic Acids Res *34*, D535-539.

Swanson, K.V., Deng, M., and Ting, J.P. (2019). The NLRP3 inflammasome: molecular activation and regulation to therapeutics. Nat Rev Immunol *19*, 477-489.

Tang, J., Tu, S., Lin, G., Guo, H., Yan, C., Liu, Q., Huang, L., Tang, N., Xiao, Y., Pope, R.M.*, et al.* (2020). Sequential ubiquitination of NLRP3 by RNF125 and Cbl-b limits inflammasome activation and endotoxemia. J Exp Med *217*.

Teo, G., Liu, G., Zhang, J., Nesvizhskii, A.I., Gingras, A.C., and Choi, H. (2014). SAINTexpress: improvements and additional features in Significance Analysis of INTeractome software. J Proteomics *100*, 37-43.

van Wilgenburg, B., Browne, C., Vowles, J., and Cowley, S.A. (2013). Efficient, long term production of monocyte-derived macrophages from human pluripotent stem cells under partly-defined and fully-defined conditions. PLoS One *8*, e71098.

Vande Walle, L., Van Opdenbosch, N., Jacques, P., Fossoul, A., Verheugen, E., Vogel, P., Beyaert, R., Elewaut, D., Kanneganti, T.D., van Loo, G., and Lamkanfi, M. (2014). Negative regulation of the NLRP3 inflammasome by A20 protects against arthritis. Nature *512*, 69-73.

Vander Linden, R.T., Hemmis, C.W., Schmitt, B., Ndoja, A., Whitby, F.G., Robinson, H., Cohen, R.E., Yao, T., and Hill, C.P. (2015). Structural basis for the activation and inhibition of the UCH37 deubiquitylase. Mol Cell *57*, 901-911.

Vaughan-Jackson, A., Stodolak, S., Ebrahimi, K.H., Browne, C., Reardon, P.K., Pires, E., Gilbert-Jaramillo, J., Cowley, S.A., and James, W.S. (2021). Differentiation of human induced pluripotent stem cells to

1342 authentic macrophages using a defined, serum-free, open-source medium. Stem Cell Reports *16*,
1343 1735-1748.
1344 Vijayaraj, S.L., Feltham, R., Rashidi, M., Frank, D., Liu, Z., Simpson, D.S., Ebert, G., Vince, A., Herold,
1345 M.J., Kueh, A.*, et al.* (2021). The ubiquitylation of IL-1beta limits its cleavage by caspase-1 and targets
1346 it for proteasomal degradation. Nat Commun *12*, 2713.
1347 Washer, S.J., Perez-Alcantara, M., Chen, Y., Steer, J., James, W.S., Trynka, G., Bassett, A.R., and Cowley,
1348 S.A. (2022). Single-cell transcriptomics defines an improved, validated monoculture protocol for
1349 differentiation of human iPSC to microglia. Sci Rep *12*, 19454.
1350 Wu, T., Hu, E., Xu, S., Chen, M., Guo, P., Dai, Z., Feng, T., Zhou, L., Tang, W., Zhan, L.*, et al.* (2021).
1351 clusterProfiler 4.0: A universal enrichment tool for interpreting omics data. Innovation (Camb) *2*,
1352 100141.
1353 Xiang, Y., Li, X., Cai, M., and Cai, D. (2023). USP9X promotes lipopolysaccharide-stimulated acute lung
1354 injury by deubiquitination of NLRP3. Cell Biol Int *47*, 394-405.
1355 Xu, T., Yu, W., Fang, H., Wang, Z., Chi, Z., Guo, X., Jiang, D., Zhang, K., Chen, S., Li, M.*, et al.* (2022).
1356 Ubiquitination of NLRP3 by gp78/Insig-1 restrains NLRP3 inflammasome activation. Cell Death Differ
1357 *29*, 1582-1595.
1358 Yan, Y., Jiang, W., Liu, L., Wang, X., Ding, C., Tian, Z., and Zhou, R. (2015). Dopamine controls systemic
1359 inflammation through inhibition of NLRP3 inflammasome. Cell *160*, 62-73.
1360 Yang, X.D., Li, W., Zhang, S., Wu, D., Jiang, X., Tan, R., Niu, X., Wang, Q., Wu, X., Liu, Z.*, et al.* (2020).
1361 PLK4 deubiquitination by Spata2-CYLD suppresses NEK7-mediated NLRP3 inflammasome activation at
1362 the centrosome. EMBO J *39*, e102201.
1363 Yu, G., Wang, L.G., Han, Y., and He, Q.Y. (2012). clusterProfiler: an R package for comparing biological
1364 themes among gene clusters. OMICS *16*, 284-287.
1365 Zangiabadi, S., and Abdul-Sater, A.A. (2022). Regulation of the NLRP3 Inflammasome by
1366 Posttranslational Modifications. J Immunol *208*, 286-292.
1367 Zhang, Z., Liu, N., Chen, X., Zhang, F., Kong, T., Tang, X., Yang, Q., Chen, W., Xiong, X., and Chen, X.
1368 (2021). UCHL1 regulates inflammation via MAPK and NF-kappaB pathways in LPS-activated
1369 macrophages. Cell Biol Int *45*, 2107-2117.
1370 Zhang, Z.R., Meszaros, G., He, W.T., Xu, Y.F., Magliarelli, H.D., Mailly, L., Mihlan, M., Liu, Y.S., Gamez,
1371 M.P., Goginashvili, A.*, et al.* (2017). Protein kinase D at the Golgi controls NLRP3 inflammasome
1372 activation. Journal of Experimental Medicine *214*, 2671-2693.

1373